DOT/FAA/TC-12/35

Federal Aviation Administration
William J. Hughes Technical Center
Aviation Research Division
Atlantic City International Airport
New Jersey 08405

Overview of Vacuum-Assisted Resin Transfer Molding Processing

June 2013

Final Report

This document is available to the U.S. public through the National Technical Information Services (NTIS), Springfield, Virginia 22161.

This document is also available from the Federal Aviation Administration William J. Hughes Technical Center at actlibrary.tc.faa.gov.

U.S. Department of Transportation
Federal Aviation Administration

NOTICE

This document is disseminated under the sponsorship of the U.S. Department of Transportation in the interest of information exchange. The U.S. Government assumes no liability for the contents or use thereof. The U.S. Government does not endorse products or manufacturers. Trade or manufacturers' names appear herein solely because they are considered essential to the objective of this report. The findings and conclusions in this report are those of the author(s) and do not necessarily represent the views of the funding agency. This document does not constitute FAA policy. Consult the FAA sponsoring organization listed on the Technical Documentation page as to its use.

This report is available at the Federal Aviation Administration William J. Hughes Technical Center's Full-Text Technical Reports page: actlibrary.tc.faa.gov in Adobe Acrobat portable document format (PDF).

Technical Report Documentation Page

1. Report No.	2. Government Accession No.	3. Recipient's Catalog No.
DOT/FAA/TC-12/35		

4. Title and Subtitle	5. Report Date
OVERVIEW OF VACUUM-ASSISTED RESIN TRANSFER MOLDING PROCESSING	June 2013
	6. Performing Organization Code
7. Author(s)	8. Performing Organization Report No.
Pit Schulze and Dirk Heider	
9. Performing Organization Name and Address	10. Work Unit No. (TRAIS)
University of Delaware Center for Composite Materials 202 Composites Manufacturing Science Laboratory Newark, DE 19716	
	11. Contract or Grant No. 04-C-AM-UD
12. Sponsoring Agency Name and Address	13. Type of Report and Period Covered
U.S. Department of Transportation Federal Aviation Administration Northwest Mountain Region – Transport Airplane Directorate 1601 Lind Avenue, SW Renton, WA 98057	Final Report
	14. Sponsoring Agency Code AIR-110

15. Supplementary Notes

The Federal Aviation Administration William J. Hughes Technical Center Aviation Research Division Technical Monitor was David Westlund.

16. Abstract

Vacuum-assisted resin transfer molding (VARTM) is an affordable process that can be readily used for large-scale composites structures. However, for many aircraft applications, VARTM does not currently provide sufficient repeatability or control of variability. Such variability is commonly observed when processing with the VARTM process. To routinely produce aircraft-quality VARTM parts, the variability must be understood.

There are many factors that influence the variability of the final part. The factors that play a major role in the cause of this variation need to be identified and the causes and effects of changes in these factors understood. This reports reviews the modeling approaches to evaluate the infusion behavior based on Darcy's law and provides the results of validation experiments. In addition, models have been developed to simulate the changes in preform thickness during and after infusion.

Three VARTM process variations were considered in this report: (1) the Seeman Composites Resin Infusion Molding Process (SCRIMP™), patented by TPI Composites, is a vacuum infusion process using a high-permeability layer to rapidly distribute the resin on the part surface and then allow through-the-thickness penetration; (2) the Controlled Atmospheric Pressure Resin Infusion Process, patented by The Boeing Company, is a VARTM variation in which a reduced pressure difference is used to minimize thickness gradients and resin bleeding; and (3) the vacuum-assisted process is another SCRIMP variation, patented by EADS, where an air-permeable membrane is used on top of the distribution media to allow continuous and areal venting, which reduces void content and creates a robust process variant.

Some initial mechanical results are presented for VARTM components manufactured using aerospace-grade materials, including toughened epoxies and carbon preforms.

17. Key Words	18. Distribution Statement
Vacuum-assisted resin transfer molding, Automation, Liquid molding	This document is available to the U.S. public through the National Technical Information Service (NTIS), Springfield, Virginia 22161. This document is also available from the Federal Aviation Administration William J. Hughes Technical Center at actlibrary.tc.faa.gov.

19. Security Classif. (of this report)	20. Security Classif. (of this page)	21. No. of Pages	22. Price
Unclassified	Unclassified	69	

Form DOT F 1700.7 (8-72) Reproduction of completed page authorized

TABLE OF CONTENTS

			Page
EXECUTIVE SUMMARY			ix
1.	INTRODUCTION		1
	1.1	Overview	1
	1.2	Significant VARTM Patent Overview	1
2.	SEEMAN COMPOSITES RESIN INFUSION MOLDING PROCESS		2
	2.1	The VARTM Process Modeling	3
	2.2	Experimental Validation	9
3.	CONTROLLED ATMOSPHERIC PRESSURE RESIN INFUSION		18
4.	VACUUM-ASSISTED PROCESS		28
	4.1	Infusion Characteristics of the VAP and SCRIMP Process	29
	4.2	Material Properties Evaluation	33
		4.2.1 Thickness Development	33
		4.2.2 Void Content and Fiber Volume Fraction Evaluation	34
		4.2.3 Mechanical Test Evaluation	35
	4.3	Membrane Material Characterization	37
	4.4	Qualitative Characterization	37
		4.4.1 Optical Microscopy	37
		4.4.2 Membrane Thickness	39
		4.4.3 Porosity of the Membranes	40
		4.4.4 Permeability of Membranes	48
5.	ELEVATED TEMPERATURE VARTM PROCESSING		51
	5.1	Materials	51
	5.2	Experimental Setup	52
	5.3	Mechanical Testing—Material Properties	55
6.	CONCLUSIONS		56
7.	REFERENCES		56

LIST OF FIGURES

Figure		Page
1	The VARTM Process is Used for Aerospace Component Production	1
2	Schematic of the SCRIMP Process	3
3	Schematic and Nomenclature Used for the Analytic Model	4
4	Mass Conservation at the Flow Front	5
5	Normalized Flow Front Shapes for the Number of Layers of Fiber Preforms	7
6	Variation in the Length of Flow Front Region *d* With Preform Thickness Predicted by the Analytical Model, for Different Values of Permeability of the Distribution Medium	7
7	The UD-CCM VARTM Test Bed That Incorporates Sensors and Enables Flow Model Validation and VARTM Automation	9
8	Experimental SmartWeave Grid With 21 Excitation and 6 Sense Lines for the 15-Layer E-Glass Preform	12
9	Arrival Time of Six-Layer 411-C50 Injection 85 cP, 40 by 6 in.	13
10	Resin Arrival Time of Nine-Layer 411-C50 Injection 85 cP, 40 by 6 in.	13
11	Resin Arrival Time of 15-Layer 411-C50 Injection 85 cP, 40 by 6 in.	13
12	Resin Arrival Time of 30-Layer 411-C50 Injection 85 cP, 40 by 6 in.	14
13	Resin Arrival Time of 40-Layer 411-C50 Injection 85 cP, 40 by 6 in.	14
14	Arrival Time of Resin at the Bottom Layer—Comparison of Model Prediction and Experimental Data From SmartWeave	15
15	Reconstructed Flow Fronts From Resin Arrival Data for 5, 9, 15, 30, and 40 Layers of Preform Material	16
16	Length of Flow Region—Comparison of Model Prediction With Experimental Observations for Different Number of Layers of Front Fiber Preform	17
17	Flow Front Profile Through the Thickness—Comparison of Model Predictions With Experimental Data for Different Number of Layers of Fiber Preform	18

18	The CAPRI Setup and Processing Steps	19
19	Out-of-Plane Air Permeability Cell Setup	20
20	Permeability as a Function of Debulking Cycle	20
21	Compaction Behavior Before and After 400 Debulking Cycles, and Thickness Change at Each Debulking Cycle Measured During Peak Vacuum	21
22	Setup to Determine Infusion and Dimensional Tolerance Parameters	22
23	Preform Pressure During Resin Infusion: Development Near the Infusion Port During Injection and Final Pressure Gradient After Full Infusion	23
24	Final Thickness Gradient After Full Infusion	24
25	Flow Profile: Surface and Tool Side	25
26	Comparison of Experimentally Obtained Lead Length and Infusion Times	27
27	The VAP Setup	28
28	Surface and Tool-Side Flow Front Comparison of the VAP and SCRIMP Processes	29
29	Infused Resin Weight as a Function of Time	31
30	The Process Robustness Experiment	32
31	Arrival Time of VAP and SCRIMP Injection on Separated L-Part	32
32	Thickness Distribution After Infusion and Cure for Both VAP and SCRIMP	34
33	Short-Beam Strength Test Results	36
34	Low Resin Permeability Creates a Resin Barrier While High Air Permeability Enables Continuous Surface Venting During VAP Processing	37
35	Scanning Electron Microscopy Image of the Cross Section of the Membrane	38
36	An SEM Image of Membrane W1 at 5000x Magnification and a Cross Section of Membrane W1 Cut by Cryomicrotoming	38
37	An SEM Image of Membrane W1 at 40,000x Magnification and an SEM Image of Membrane D at 10,000x Magnification	39

38	An SEM Image of Support W at 55x Magnification and an SEM Image of the Donaldson Support at 35x Magnification	39
39	An SEM of the Membrane W1 Cut by Cryomicrotoming and Close-Up	40
40	Methodology to Calculate the Pore Occurrences	42
41	Pore Size Distributions of W1, WA, and WB	43
42	Pore Size Distributions of D2, D1, and D4	43
43	Pore Size Distributions of all Six Membranes	44
44	Optimization of Pore Size Distribution Through Fit of Flow Rates	45
45	LabVIEW Interface to Obtain the Pore Size Distribution	46
46	Pore Size Distribution for Membrane W	47
47	Pore Size Distribution for Membrane D	47
48	Pore Size Distribution for all Six Membranes	48
49	Permeability of the Six Membranes With Water	50
50	Permeability of the Six Membranes With Cycom 977-20 Resin	51
51	Process Temperature Profile for Cycom 977-20 With PriForm Reinforcement	52
52	The ET-VARTM Work Cell Schematic	52
53	Viscosity Profile of Cycom 977-20 During Two-Step Temperature Cycle	53
54	Viscosity Profile of Cycom 977-20 During Three-Step Temperature Cycle	53
55	Viscosity Profile of Cycom 977-20	54
56	Initial Laminate Quality Showing Heavy Macrovoid Formation and Improved Laminate Quality With Virtually No Void Formation After Increasing Infusion Speed	55

LIST OF TABLES

Table		Page
1	Patent Overview	2
2	Nomenclature Used in the Analytical Model	6
3	Measured Material Properties of Fiber Preform and Distribution Medium	11
4	Input Properties for the Analytical VARTM Model	26
5	Parameters for Flow Model	30
6	Fiber Volume Fraction and Void Content With and Without Degassing of Resin	35
7	Summary of VAP Benefits	36
8	Thickness of Membranes	40
9	Porosity of Membranes	40
10	Maximum Pore Size of Membranes	41
11	The MFP Size of Membranes	42
12	Probability Density and Cumulative Distribution Functions for the Weibull Fit	45
13	Weibull Parameters for All Membranes	47
14	Viscosity and Surface Tension of the Fluids of Interest	49
15	Contact Angles Fluids and Membranes	49
16	Mechanical Test Results	55

LIST OF ACRONYMS

1D	One-dimensional
2D	Two-dimensional
3D	Three-dimensional
BP	Bubble point
CAPRI	Controlled Atmospheric Pressure Resin Infusion
CCD	Charge-coupled device
CV	Coefficient of variation
ET-VARTM	Elevated Temperature VARTM
MFP	Mean flow pore
PTFE	Polytetrafluoroethylene
RTM	Resin transfer molding
SCRIMP	Seeman Composites Resin Infusion Molding Process
SEM	Scanning electron microscopy
UD-CCM	University of Delaware-Center for Composite Materials
VAP	Vacuum-Assisted Process
VARTM	Vacuum-Assisted Resin Transfer Molding

EXECUTIVE SUMMARY

This report details the work conducted at the University of Delaware-Center for Composite Materials (UD-CCM) on the vacuum-assisted resin transfer molding (VARTM) process characterization and optimization. A comprehensive literature and patent review was conducted, and the most important variants of the VARTM process—Seeman Composites Resin Infusion Molding Process, Controlled Atmospheric Pressure Resin Infusion (CAPRI), and vacuum-assisted process (VAP®)—were investigated in detail.

The current process modeling approach based on Darcy's Law was evaluated in experiments using the UD-CCM VARTM test bed with integrated SmartWeave® technology. The demonstrated complex, three-dimensional flow behavior underlined the importance of developing on-line sensing, control, and optimization for VARTM processes.

The effect of processing via CAPRI and VAP on preform and laminate parameters (i.e., permeability, thickness gradients, fiber/void fraction, and mechanical properties) was studied. Specific to VAP processing, different membrane materials were characterized and evaluated.

The report provides a framework to evaluate existing VARTM processes as well as newly developed approaches. It outlines the key advantages and disadvantages and provides a fundamental understanding of the process physics.

1. INTRODUCTION.

1.1 OVERVIEW.

Vacuum-assisted resin transfer molding (VARTM) offers numerous cost advantages over traditional resin transfer molding (RTM) due to lower tooling costs, potential for room temperature processing, and scalability for large structures. Historically, the wind energy and marine market used this process to produce high-performance composite components. Low-process repeatability and dimensional tolerances compared to autoclave processing, as well as lower materials performance of the resin versus prepreg, limited its aerospace applications. Recently, an improved understanding of the process physics combined with advances in infusible, toughened epoxies [1-3] and automation equipment enabled consideration for using the process for structural aerospace components. Technology demonstrators, such as the Boeing C-17 main landing gear door and forward pylon of the Chinook CH-47, met performance requirements for military components, while multiple primary structural components for civil air transportation, such as the Airbus A380 flap tracks and the Boeing 787 pressure bulkhead, are currently in production and manufactured with the VARTM/vacuum-assisted process (VAP) process (figure 1).

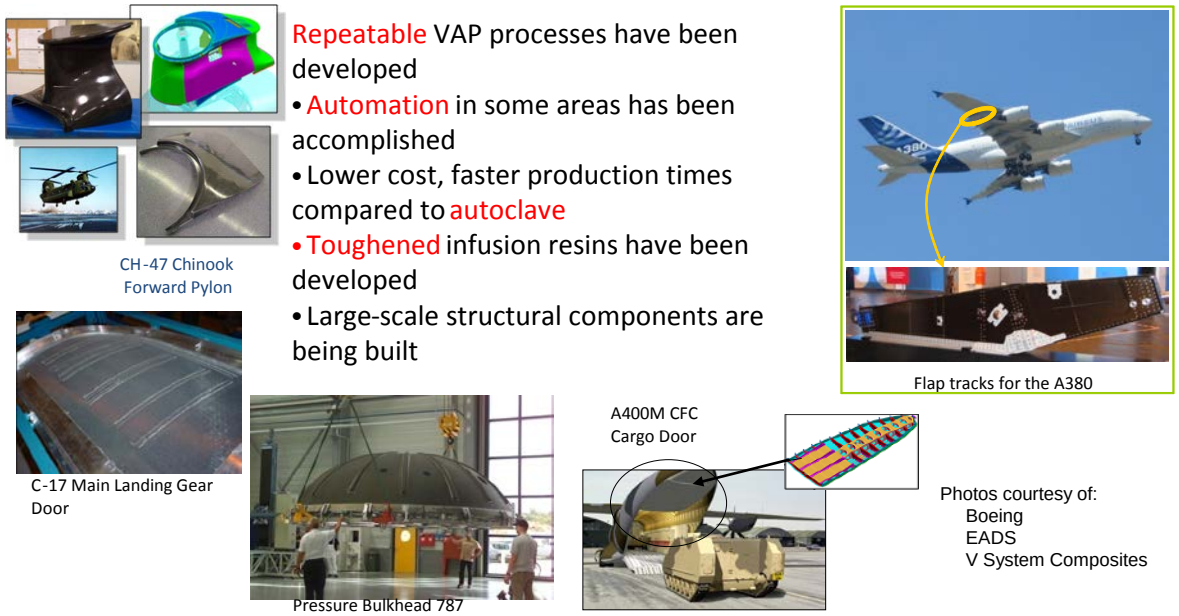

Figure 1. The VARTM Process is Used for Aerospace Component Production

1.2 SIGNIFICANT VARTM PATENT OVERVIEW.

Many patents have been granted (table 1) with the same underlying principle of pulling liquid matrix material through the infusion ports into a sealed, dry fiber preform. Compaction of the reinforcement and pressure gradient needed for resin flow is provided by applying a vacuum on the opposite side of the preform (vent). Three significant process variations are explained in detail in this report: (1) the Seeman Composites Resin Infusion Molding Process (SCRIMP®),

patent held by TPI Composites; (2) the VAP, patent held by EADS; and (3) Controlled Atmospheric Pressure Resin Infusion (CAPRI), patent held by The Boeing Company.

Table 1. Patent Overview [4]

Muskat	1950	2,495,640	Marco method
Smith	1959	2,913,036	Process and apparatus for molding large plastic structures
Geringer	1964	3,137,898	RTM
Muskat	1967	3,342,787	RTM
Group Lotus	1972	(GB) 1,432,333	Vacuum molding patent
Johnson	1979	4,132,755	Process for manufacturing resin-impregnated, reinforced articles without the presence of resin fumes
Rolston	1980	4,238,437	Method for producing fiber reinforced product
Fourcher	1982	4,312,829	Molding method
Palmer	1982	4,311,661	Resin impregnation process
Lecomte	1982	4,359,437	Method and apparatus for producing a thin- walled article of synthetic resin, in particular a large-sized article
Letterman	1986	4,622,091	Resin film infusion process and apparatus
Krauter	1988	4,759,893	Method of making FRP molded parts
Epel	1989	4,873044	Method and apparatus for reduction of mold cycle time
McGowen	1989	4,886,442	Vacuum bag tooling app. with inflatable seal
Seemann	1990	4,902,215	Plastic transfer molding techniques for the production of fiber reinforced plastic structures
Palmer	1990	4,942,013	Vacuum resin impregnation process
Lindgren	1990	4,975,311	Vacuum lamination station
Bailey	1995	5,588,392	Resin Transfer molding process (for boat hulls)
Seemann	1995	5,439,635	Unitary vacuum bag for forming fiber reinforced composite articles and process for making same
McGuiness	1996	5,526,767	Method of manufacturing a boat hull

2. SEEMAN COMPOSITES RESIN INFUSION MOLDING PROCESS.

The SCRIMP [5] is a patented VARTM variation with a highly permeable distribution medium incorporated as a surface layer on the preform. During infusion, the resin flows preferentially across the surface and simultaneously through the preform thickness, enabling large parts to be fabricated. The surface flow front leads the tool flow front, and the lead length can be significant for thick preforms. Resin infusion times increase exponentially with injection length during VARTM processing. During sequential injection processing, several infusion tubes are located on the distribution media, and the injection lines are sequentially opened to minimize cycle times. Sequential injection reduces the injection length to the distance between the resin gates, which effectively divides the part in multiple injection regions. As the vacuum is applied, usually on the opposite end of the preform, the flow in the VARTM process is a three-dimensional (3D) flow through anisotropic porous media (i.e., preform). The lay-up of the materials used in the process is shown in figure 2. In this process, large parts can be infused rapidly using a variety of resins, including vinyl esters, phenolics, and epoxies, at room temperature under vacuum pressure. Also, new, toughened aerospace epoxy resins have been developed and allow infusion at slightly elevated temperatures followed by a high-temperature cure.

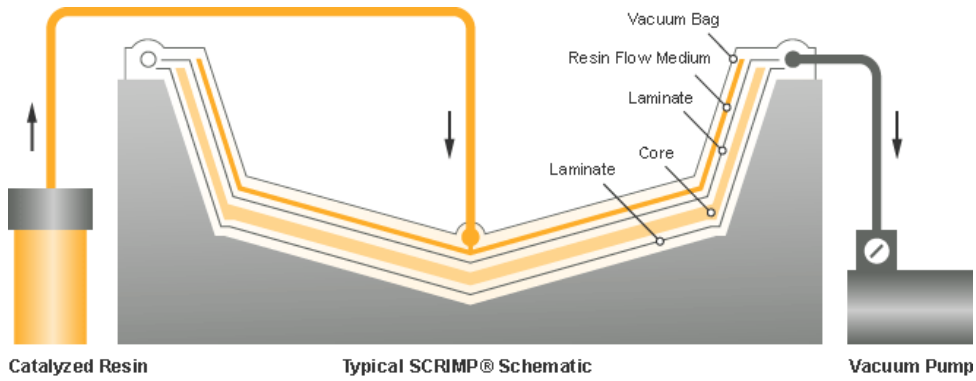

Figure 2. Schematic of the SCRIMP Process [6]

VARTM is a closed process offering environmental benefits through reduced emission of volatile organic compounds. In very large composite structures, multiple inlet gates are required to ensure complete wet-out of the part prior to gelation of the resin. Selection of distribution media, preforms, and gate and vent locations are typically based on past experience for similar applications. New applications in which part thickness, resin properties, or preform characteristics will change require costly trial-and-error process development. Hence, a fundamental understanding of the process physics and associated process models needs to be established and experimentally validated.

Understanding the flow during the impregnation process provides insight into tool design, gate, vent, and sensor placement that can affect part quality. In addition, modeling and simulation of the flow can enable optimization of the process design variables, such as the cycle time and the distance between resin inlets as a function of the permeabilities of the distribution medium and the fiber preform, resin viscosity, and preform thickness.

2.1 THE VARTM PROCESS MODELING.

The flow of resin through porous media, such as fiber preforms and resin distribution media, is governed by Darcy's Law.

$$u = \frac{-K}{\mu} \cdot \nabla P \tag{1}$$

Here, u is Darcy's velocity, which is defined as the total flow rate per total cross-sectional area, K is the permeability tensor, which characterizes the ease of flow through the fiber preform, and μ is the viscosity of the resin. This, when coupled with the continuity equation for incompressible flow, gives the Laplace's equation for the fluid pressure field inside a region permeated by the fluid.

$$\nabla \cdot (\frac{K}{\mu} \cdot \nabla P) = 0 \tag{2}$$

The flow simulations can be either two-dimensional (2D) or 3D. In 2D flow modeling [7-13] the flow of resin through the thickness is considered uniform, and the finite element discretization is applied along the other two directions. One such simulation is the liquid injection molding Simulation, which is based on the finite element control volume approach [14]. In 2D simulations, only the permeabilities in the plane of interest are required. In 3D simulations [15], the pressure and flow in all three directions is solved, and a 3D permeability tensor is required. Resin infusion process simulation is one such 3D simulation based on finite element methods without using the control volume approach [16]. Usually, the geometry, the material parameters, and the position of resin inlets and outlets are specified before the filling simulation is carried out.

Closed-form analytical solutions have also been derived for the resin flow under simplifying assumptions and for simple geometries and preforms. These solutions explain the role of various process variables (such as vacuum levels, material properties, and preform thickness) and their interactions during processing. Indeed, a closed-form solution of the resin flow during the VARTM process not only enables parametric studies, optimization, and reduction of computational expenses of full-scale simulations, but it also offers insight into scalability by identifying appropriate distribution media and resin injection inlet spacings for a required preform, resin system, and the part dimensions.

A closed-form solution for the flow of resin in the VARTM process was derived [17]. The analytical solution for 2D porous media focuses on a representative cross section (x-y plane shown in figure 3) consisting of the distribution layer (the high-permeability material) and the structural layer (the preform material). It is assumed that the flow is well developed and can be divided into two regimes: a saturated region with no through-the-thickness flow and a flow front region where the resin is infiltrating into the preform from the distribution medium.

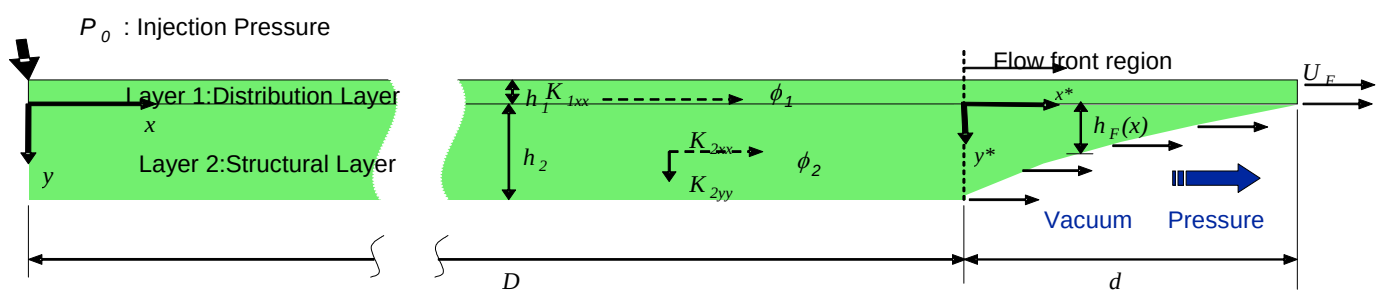

d: region with transverse flow = flow front length
D: region without transverse flow = length behind the flow front re
U_F: flow front velocity
μ : Viscosity of Resin

Figure 3. Schematic and Nomenclature Used for the Analytic Model

As shown in figure 3, the lay-up of materials is modeled as two distinct layers of permeable materials. The distribution layer (layer 1) is much thinner than the structural layer (layer 2), such that $h_1 << h_2$, where h_1 and h_2 are the respective thickness of the two layers. The flow front in

the distribution layer is considered uniform (i.e., no gradients in the thickness direction) as the permeability is isotropic for the distribution layer. The permeability of the distribution layer is K_{1xx} along and across the flow direction, and the permeabilities of the structural layer are K_{2xx} and K_{2yy} in the x and y directions, respectively. The resin viscosity is μ. Vacuum is applied to the flow front, and the flow is driven by the constant pressure difference, P_0, between the pressure at the inlet, which is atmospheric pressure, and the vacuum pressure at the flow front.

In the saturated region, the flow is one-dimensional (1D) with Darcy's velocities U_1 and U_2 in layers 1 and 2, respectively. The length of this saturated region is D, and the pressure at the boundary with the flow region is assumed to be P_D. The second region, shown in figure 4, is the flow front region where there is transverse flow from the distribution layer to the structural layer. The flow front region, of length d, is assumed to maintain its shape, given by $h_F(x)$ and advances with a uniform horizontal velocity of U_F. This is the observed velocity of the resin and not the Darcy's velocity. The transverse velocity of resin infiltration from the distribution layer into the structural layer is u_{12y}. The horizontal velocity in the flow front region in the distribution layer is denoted by u_{1x} and at the distance $x = (D + d) = \Phi_1 U_F$.

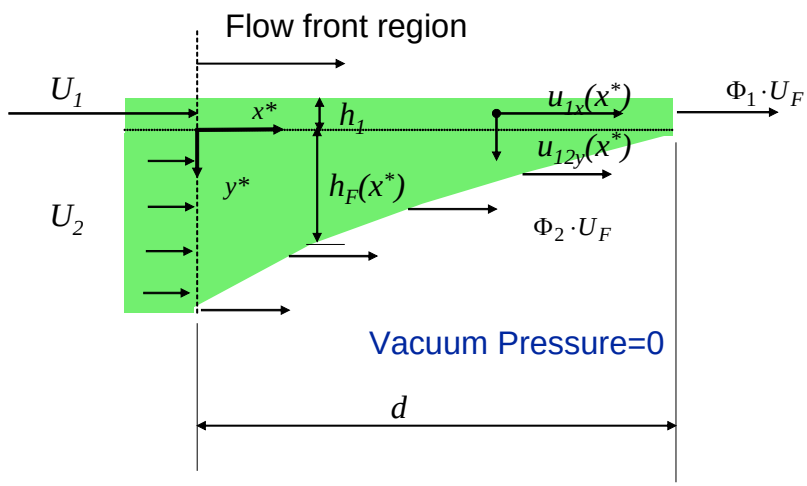

Figure 4. Mass Conservation at the Flow Front

The flow front region is assumed to be fully developed and moves with a uniform velocity. The law of conservation of mass and Darcy's law for flow through porous media are applied in each region. The resulting equations are nondimensionalized and are solved to yield the flow front shape and the development of the saturated region with time. The flow front shape and the time to fill length D of the preform are given in equations 3 through 5, respectively. The nomenclature used is summarized in table 2.

Table 2. Nomenclature Used in the Analytical Model

Symbol	Definition
$h_F^*(x^*)$	Flow front shape as a function of distance from the saturated region, x^*
t-t_0	Time to fill saturated length D of the part
D	Length of saturated region
d	Length of flow front region
U_F	Flow front velocity
U_2	Flow velocity in saturated region in the preform layer
Φ_1	Porosity of the distribution medium
Φ_2	Porosity of the fiber preform
K_{1xx}	Permeability of distribution layer in the direction of flow
K_{2xx}	Permeability of preform layer in the direction of flow
K_{2yy}	Permeability of preform layer in the direction transverse to the flow
μ	Viscosity of the resin

The variation of the flow front shape with different numbers of layers of fiber preform in the structural layer is shown in figure 5.

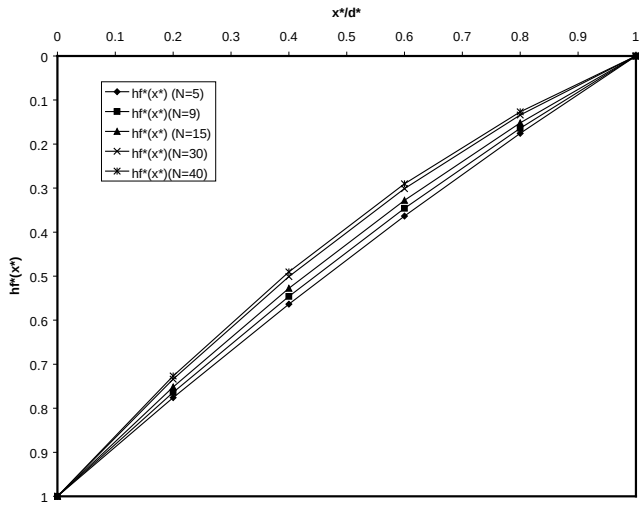

Figure 5. Normalized Flow Front Shapes for the Number of Layers (N) of Fiber Preforms

A parametric study of the length of flow front region *d* demonstrating the effect of the change in permeability of the distribution medium is shown in figure 6.

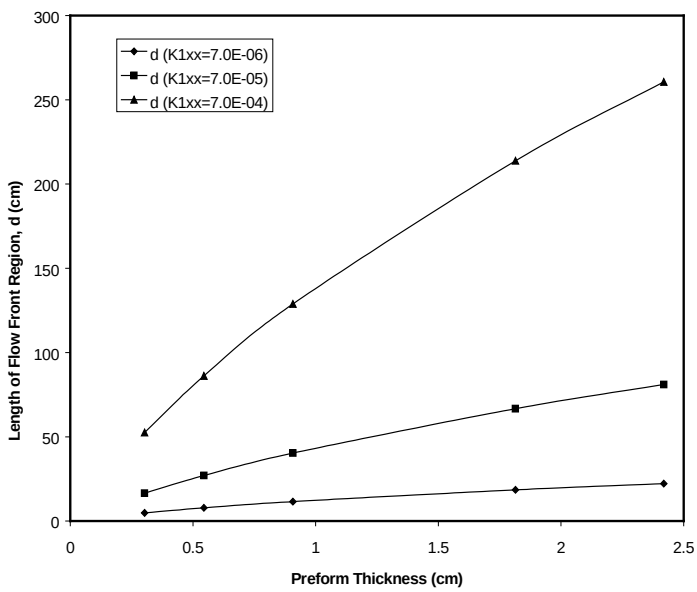

Figure 6. Variation in the Length of Flow Front Region *d* With Preform Thickness Predicted by the Analytical Model, for Different Values of Permeability of the Distribution Medium (A typical permeability value for the distribution medium is 7.0E-05.)

Analytical prediction of the saturated region's (*D*) length with time, the length of the flow front region (*d*), and the shape of the flow front ($h_F(x)$) are compared to experimental measurements of these parameters as a function of the preform thickness in the next section.

$$h_F^*(x^*) = \frac{K_{2yy}^*}{6h_1^*} x^{*2} - \sqrt{\frac{2K_{2yy}^*}{3h_1^*} + \frac{\Phi_1 K_{2yy}^*}{\Phi_2 - U_2^*}} x^* + 1 \tag{3}$$

$$t - t_0 = C_1(D^2 - D_0^2) + C_2(D - D_0) \tag{4}$$

$$d^* = \frac{3h_1^*}{\sqrt{K_{2yy}^*}} \left(\sqrt{\frac{\Phi_1}{\Phi_2 - U_2^*} + \frac{2}{3h_1^*}} - \sqrt{\frac{\Phi_1}{\Phi_2 - U_2^*}} \right) \tag{5}$$

Where

$$U^* = \frac{U}{U_F}$$

$$K^* = \frac{K}{K_{1xx}}$$

$$h_F^* = \frac{h_F}{h_2}$$

$$x^* = \frac{x - D}{h_2}$$

$$h_1^* = \frac{h_1}{h_2}$$

$$d^* = \frac{d}{h_2}$$

$$P^* = \frac{P}{P_0}$$

$$U_2^* = \frac{(\Phi_1 h_1^* + \Phi_2)}{(\frac{h}{K_{1xx}^*} + 1)}$$

$$\Gamma = \frac{U_2^*}{K_{2xx}^*}$$

$$\Lambda = \frac{(\Phi_2 - U_2^*)}{K_{2yy}^*} \sqrt{\frac{2K_{2yy}^*}{3h_1^*} + \frac{\Phi_1 K_{2yy}^*}{\Phi_2 - U_2^*}}$$

$$C_1 = \frac{\Gamma \mu}{2K_{1xx} P_0}$$

$$C_2 = \frac{\mu \Lambda h_2}{K_{1xx} P_0}$$

2.2 EXPERIMENTAL VALIDATION.

The UD-CCM VARTM test bed (figure 7) was built to sense and control the critical process parameters [18 and 19]. In particular, monitoring the resin arrival times and flow rates, as well as tightly controlling the applied vacuum levels, is needed to study the resin flow behavior during preform impregnation and to validate process models. The vacuum control system consists of a TESCOM™ ER3000 pressure controller, a VACCON™ VDF250 variable flow vacuum pump (venturi pump), and a VACOON™ VSSA vacuum sensor for each individual vent. A separate air compressor is needed due to the high flow rates required by the venturi pumps to maintain the desired inlet pressure at each pressure controller. The pressure controller adjusts the pressure to the venturi pump, which generates the vacuum. The vacuum level is measured in situ with the vacuum sensor and is used in a feedback loop to adjust the pressure controller. Together, this system provides accurate and fast control of the vacuum level in the vacuum tank and in the preform near the vent location. A graphical user interface written in LabVIEW gives easy access to the control variables and sensor feedback.

Figure 7. The UD-CCM VARTM Test Bed That Incorporates Sensors and Enables Flow Model Validation and VARTM Automation

Two systems were used to accurately monitor the resin flow behavior. A Pulnix TM-1001 charge-coupled device (CCD) camera captures, in real time, the resin flow on the preform surface. Each individual picture is preprocessed to reduce the pixel noise, and subsequently, a threshold algorithm is applied to calculate the wet-out location in the preform. An arrival time map is continuously updated and can be used on- or offline to calculate the resin position over time. A second monitoring system is based on SmartWeave® [20 and 21] technology. An orthogonal grid of wires (sense and excitation lines) was used to sense the flow front location. The resistance at each grid point between one excitation and one sense was measured using a voltage divider system and a data acquisition board from National Instruments™. The junction resistance drops significantly upon resin arrival and indicates the preform wet-out at each location. The current UD-CCM SmartWeave system enables point sensors to be multiplexed within a 64 by 64 sensor grid. Multiple grids are placed between different layers of the preform to enable 3D flow monitoring during impregnation.

The experimental work consisted of two parts: (1) the measurement of model input properties, such as the permeabilities of the preform and distribution media; and (2) flow front measurement with varying preform thickness to validate model predictions. The material properties required by the model include the permeabilities and porosities of the structural layer (e.g., fiber preform (K_{2xx}, K_{2yy}, and Φ_2) and distribution medium (K_{1xx} and Φ_1)), and the resin viscosity (μ). The resin used in this study was Dow Derakane 411-C50 vinyl ester. The fiber preform and the distribution layer were made from 24-oz E-glass woven fabric and a single layer of shading material from Roxford Fordell. Permeability measurement experiments were conducted to measure the permeabilities using the test bed [22]. The porosities were determined using the standard ASTM D2584 [23] burn-off test.

The permeability tensor of the fiber preform has three principal values, k_1, k_2, and k_3. In earlier work, a method to predict all three principal components in one experiment using SmartWeave was developed [22]. This method was used for the determination of the preform permeability values required for this study. For the material used here (E-glass fabric), the x, y, and z directions coincide with the principal directions. In the experiment to measure these values, 10 to 20 layers of the preform were placed under vacuum, without the distribution medium. A number of SmartWeave layers were used at regular spacing between the layers. Bare copper wires were used to minimize the interference on the flow front, and a video camera recorded the flow front on the surface of the fiber preform. In this experiment, the data were obtained by the SmartWeave system at the nodes of the intersecting grid of wires. When the flow front reached the node at coordinates $x_i^{'}$, $y_i^{'}$, $z_i^{'}$, and t_i, the time was recorded. According to theory, one can relate the arrival times with the preform permeability as detailed in reference 22.

$$t_{ff,i} = f(k_1, k_2, k_3, k) \tag{6}$$

where

$$k = (k_1 k_2 k_3)^{\frac{1}{3}}$$

These nonlinear equations were solved to obtain the values of k_1, k_2, and k_3, as given in reference 22, and the central injection method was used to inject resin into the preform. An inhibitor was used to prevent the premature cure of the resin. The data from the experiment consisted of the flow rate, the video of the flow front on the surface, and the time to reach each SmartWeave node through the thickness. Additional data included the resin properties (density and viscosity), the size of the injection tube, and the level of vacuum used. The resulting permeability values are shown in table 3.

Table 3. Measured Material Properties of Fiber Preform and Distribution Medium

K_{1xx}	7.00E-05 m^2
K_{2xx}	3.63E-07 m^2
K_{2yy}	9.20E-09 m^2
ϕ_1	0.9
ϕ_2	0.5
μ	85 cP

The permeability of the distribution medium was measured using an independent 1D flow experiment. The distribution medium was placed under vacuum, and the resin was injected into a line injection source at one end. A video of the flow front progression with time was used for determining the permeability. The distance covered by the flow with time was recorded and the permeability was determined using the 1D flow equation.

$$K_{1xx} = \frac{\mu x_f^2}{2 * t * \Delta P} \tag{7}$$

A 40-inch-long section was bagged and injected using vinyl ester 411-C50 resin. The 40-inch-long panel spanned 650 pixels of each image, resulting in a resolution of approximately 0.06 inch per pixel. The arrival times of the resin for each image pixel were determined from the video of the flow front. Equation 7 was applied to calculate the permeability of the distribution media. The permeability values of the preform and the distribution medium are shown in table 3.

Since the volume fractions (and preform porosities Φ_1 and Φ_2) of the materials change under compaction by vacuum, it was necessary to estimate them using the fabricated panels. The ASTM D2584 standard [23] burn-off test was used to measure the volume fractions of the fiber preforms and distribution.

Flow experiments were conducted to measure the following parameters:

- Time to fill a particular length of composite (t-t_0)
- Length of flow front region (d)
- Shape of flow front ($h_F^*(x^*)$)

In these experiments, preform thickness was varied by increasing the number of layers of fiber preform (6, 9, 15, 30, and 40 layers, in which one ply is approximately 1/42 in. thick). The 3D flow information was generated from the CCD camera that records the flow front at the top surface and from the SmartWeave embedded at regular intervals throughout the thickness (see figure 8). In general, flow front information is measured at a minimum of three locations through the thickness of the fiber preform.

Five different composite panels were manufactured with 6, 9, 15, 30, and 40 layers of 24-oz E-glass woven fabric. One layer of shading material from Roxford Fordell was used as the distribution media. The dimensions of each panel were 40 in. long and 6 in. wide. Twenty-one excitation lines, at 2-in., were placed on top of the distribution media, and one sense line was placed at mid-width every 3 layers for the 6-, 9-, 15-layer parts and 5 layers for the 30- and 40-layer preforms, respectively. This allowed for accurate through-the-thickness flow measurements with up to 168 sensor locations.

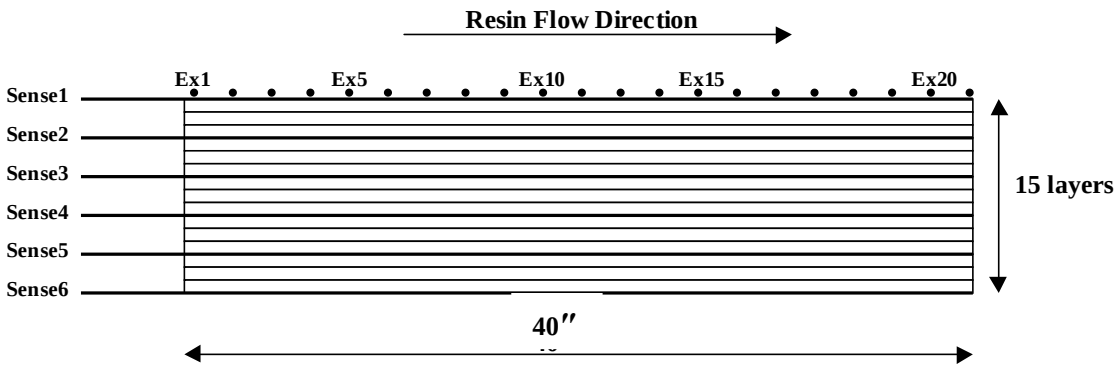

Figure 8. Experimental SmartWeave Grid With 21 Excitation and 6 Sense Lines for the 15-Layer E-Glass Preform

The properties of the materials used for the experiments were measured, and the results are summarized in table 2. Note that the permeability of a single layer of distribution medium is 2 to 4 orders of magnitude higher than the preform. The relative magnitude of the permeabilities clearly indicates that the path of least resistance will initially be in the distribution medium. Furthermore, since $K_{2yy} << K_{2xx} << K_{1xx}$, significant gradients in the flow front region will be developed with increasing preform thickness.

Using the experimental procedure outlined above, the resin arrival times were recorded throughout the preform. The experimental results are shown in figures 9 through 13 for preforms containing 6, 9, 15, 30, and 40 layers, respectively. A number of observations were made from these results. The overall fill time increases significantly as the preform thickness increases, ranging from 200 to 1000 seconds for the 6- to 40-ply preforms (the break in figures 9 and 10 is due to the failure of a line of sensors during the injection). The fill time is approximately a linear function of the preform thickness. As shown in these figures, in all cases, the resin arrival time at the bottom layer lags behind the top surface due to the presence of the high-permeability layer. The lag time also increases significantly, from 10 to more than 600 seconds, with increasing preform thickness.

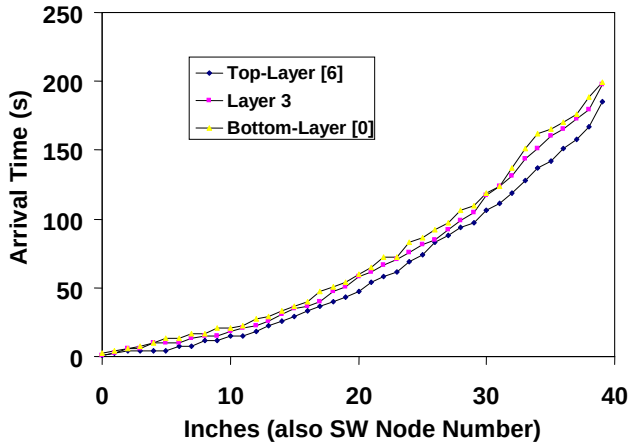

Figure 9. Arrival Time of Six-Layer 411-C50 Injection 85 cP, 40 by 6 in.

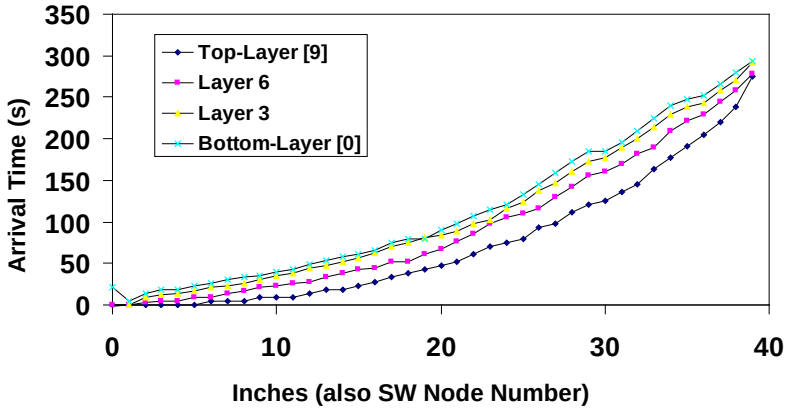

Figure 10. Resin Arrival Time of Nine-Layer 411-C50 Injection 85 cP, 40 by 6 in.

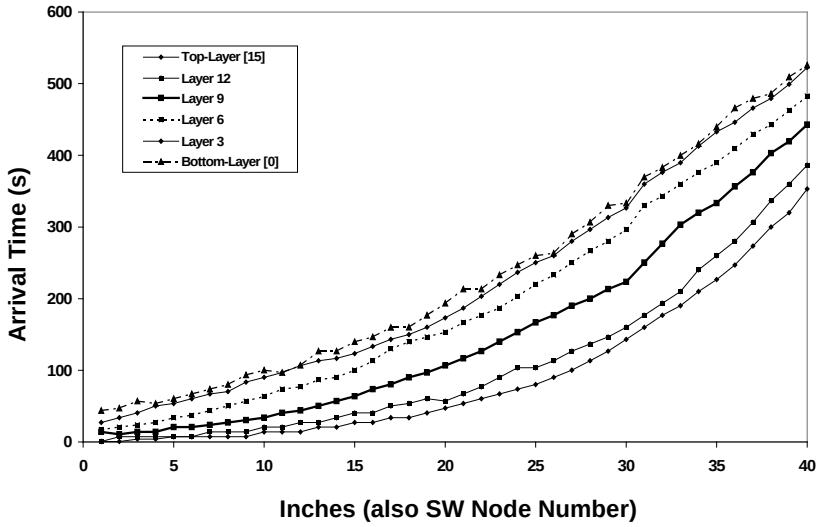

Figure 11. Resin Arrival Time of 15-Layer 411-C50 Injection 85 cP, 40 by 6 in.

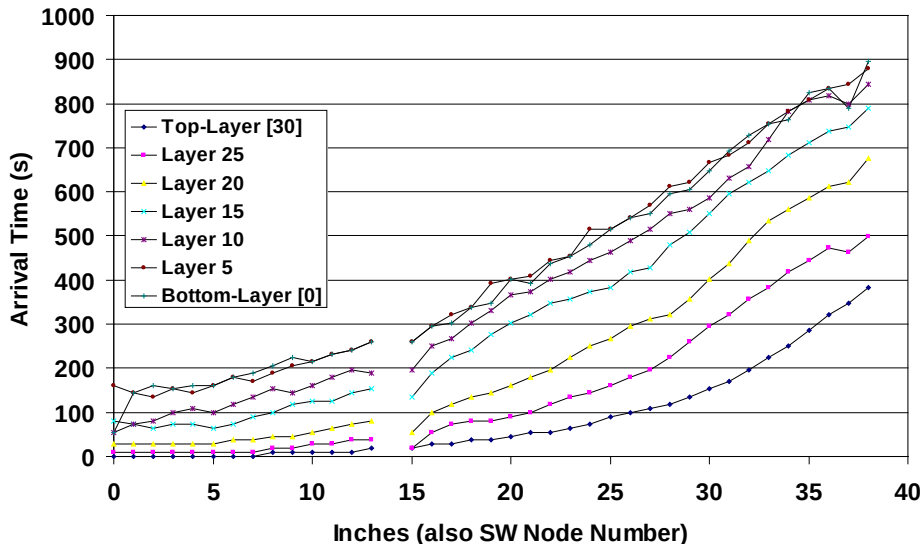

Figure 12. Resin Arrival Time of 30-Layer 411-C50 Injection 85 cP, 40 by 6 in.

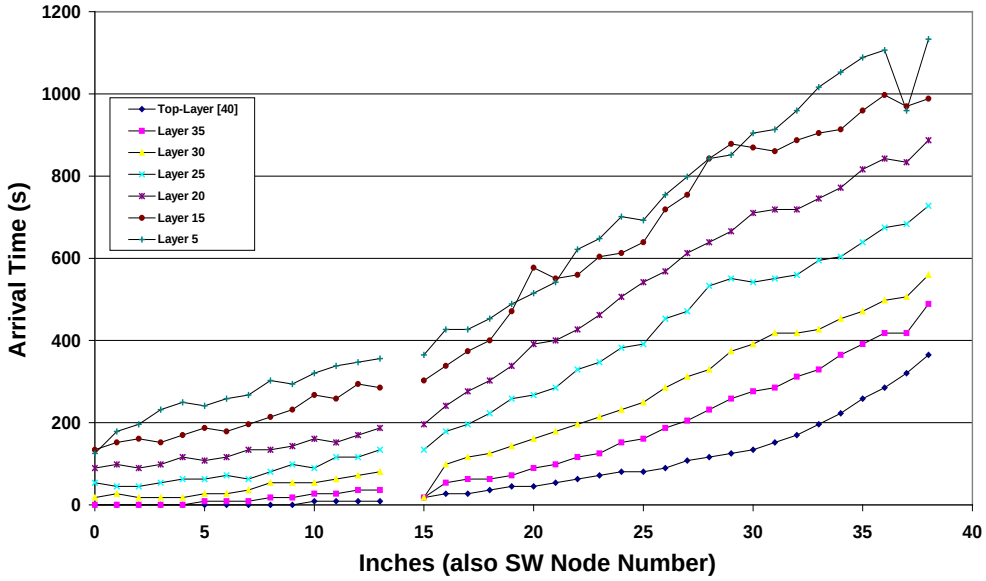

Figure 13. Resin Arrival Time of 40-Layer 411-C50 Injection 85 cP, 40 by 6 in.

The experimentally measured arrival time for the bottom layer was equivalent to the time taken to fill the saturated region predicted by the model. In figure 14, model predictions are correlated with experimental measurements over the full range of the preform thickness. The properties of the resin and fiber preform from table 3 were used for the comparison. The times to fill the bottom layer were compared with those computed using equation 3. Overall, the model accurately predicted the time to fill the preform layer. This also implies that the independent measurement of the permeabilities, porosities, and the resin viscosity were accurate as well. For the thicker preform, some discrepancy was noticed for regions near the inlet where steady-state flow may not have been achieved.

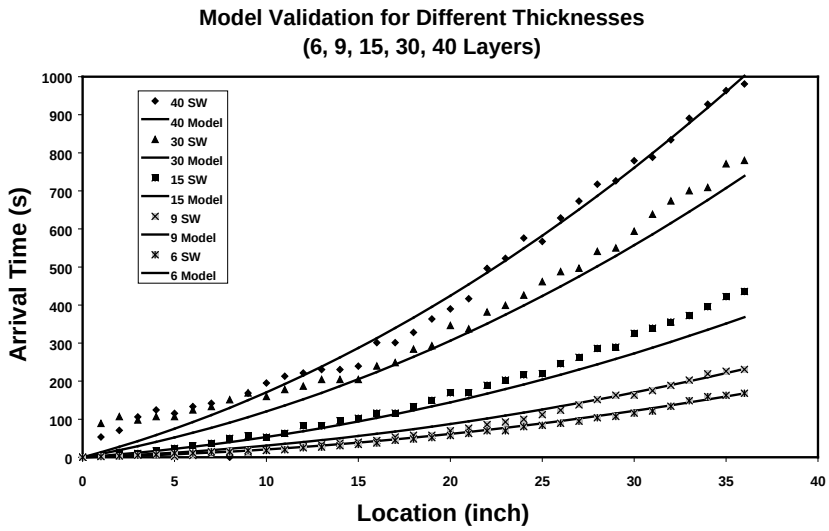

Figure 14. Arrival Time of Resin at the Bottom Layer—Comparison of Model Prediction and Experimental Data From SmartWeave

Given the location of flow sensors in the preform, arrival times can be used to reconstruct the flow fronts. These results are presented in figure 15. Consistent with the description of lag time, the flow front at the bottom lags behind the flow front at the surface. This lag distance ranges from 3/4 in. for the 6-ply preform to more than 24 in. for the 40-ply preform. This is a significant result because standard industrial practice calls for an inlet spacing of 18 in., which is suitable for thin preforms (when the lag distance is smaller than the inlet spacing), but it should be reassessed for thick preforms, when the lag distance is of the same order of magnitude and often larger than the standard inlet spacing.

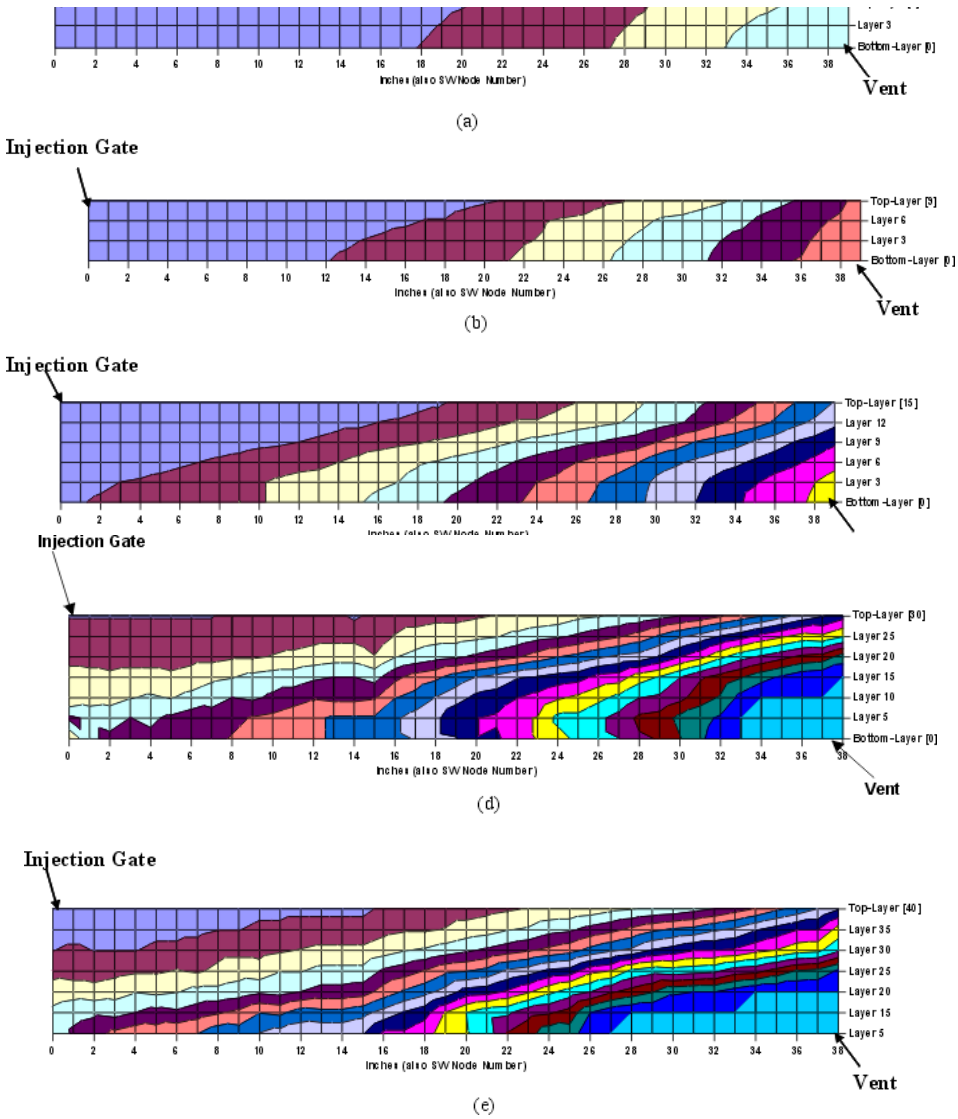

Figure 15. Reconstructed Flow Fronts From Resin Arrival Data for (a) 5, (b) 9, (c) 15, (d) 30, and (e) 40 Layers of Preform Material

The sensor information was integrated into a complete picture of the resin flow and shows that the resin flow in the VARTM process has an initial transition region near the injection location and a steady flow front shape thereafter. The variations in the flow front shape may be caused by local property variations and also due to the discrete nature of the SmartWeave grid. The length of the flow front and, hence, the lag between resin arrivals at the top and bottom layers increase with the increase in the number of layers, and consequently, with the increase in the thickness of the preform.

The lag distance, *d*, was measured from the experimental data and was compared to that predicted by the analytical model. The results are presented in figure 16. The length of the flow front region also shows good agreement with the model predictions. The length observed from the experiment is always less than that predicted by the model. This is because the model divides

the flow into two separate regions—the flow front region and the saturated region. Whereas, there are transition regions at the injection location and between the flow front and saturated regions, as demonstrated by the simulation studies [17]. In effect, the model incorporates the mass flow in these transition regions into the flow front region, thus overestimating the length of the flow front region, *d*. The locations of the flow front $h_F(x)$ at any given time was tracked from the experimental data and compared with those predicted by the analytical model.

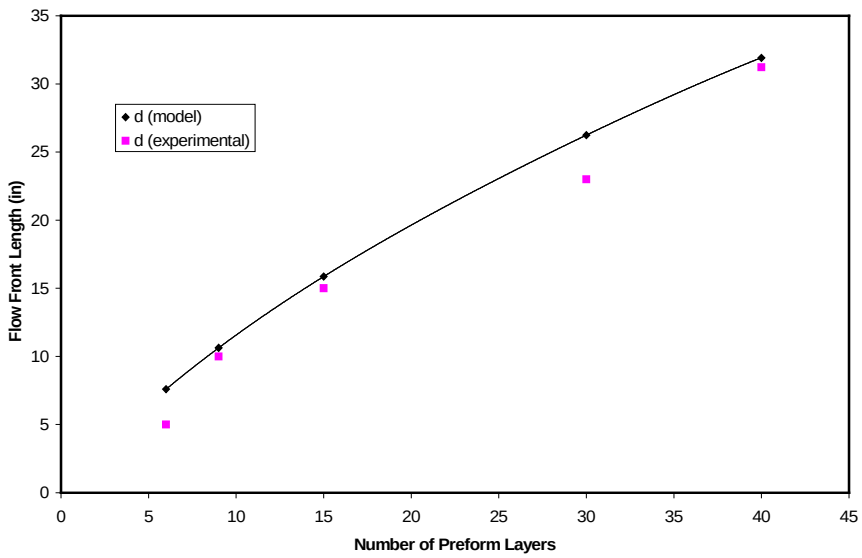

Figure 16. Length of Flow Region—Comparison of Model Prediction With Experimental Observations for Different Number of Layers of Front Fiber Preform

In figure 17, the locations of the flow front profile from experiment and the model are plotted for each case study used in the experiment. It can be observed that the flow front locations from the experiments are always less than those predicted by the model for any given x^*/d (model). This is due to the overestimation of the flow front region length by the analytical model. It can also be observed that the experimental data are closer to the flow front predicted by the analytical model as the number of layers of preform increase. This is consistent with the development of the model in which the thickness of the distribution medium is assumed to be significantly smaller than the structural (fiber preform) layer. As the number of fiber layers increases, the accuracy of the analytical model increases and, hence, the better match between experimental flow front data and the model predictions.

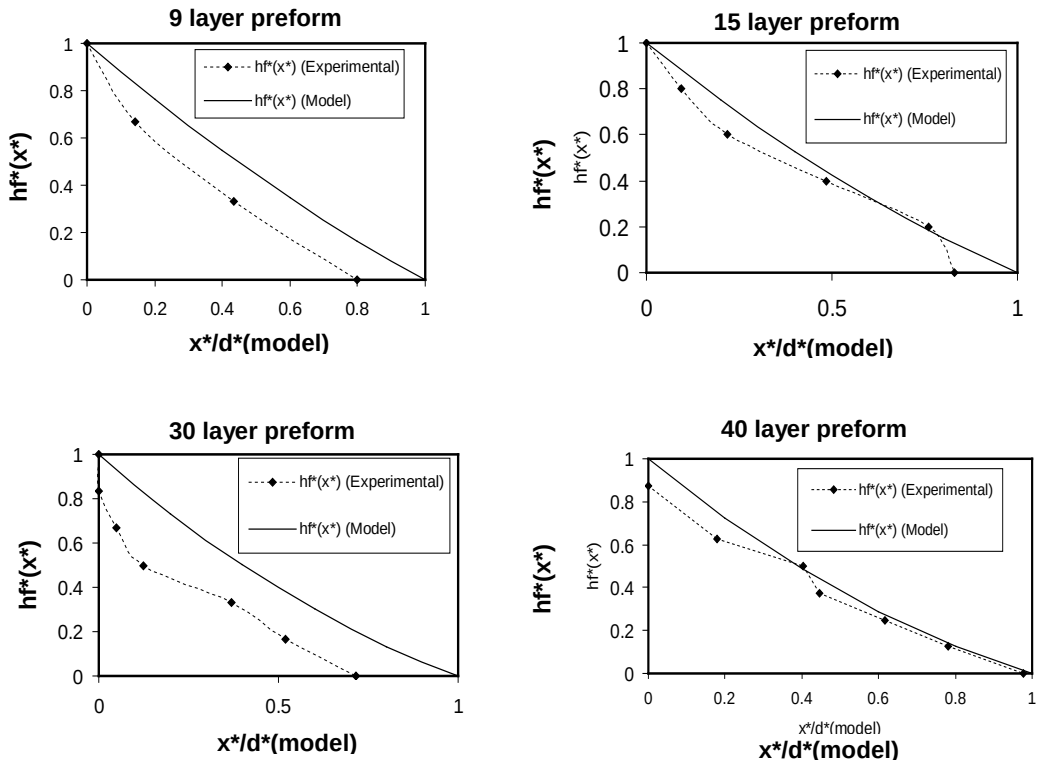

Figure 17. Flow Front Profile Through the Thickness—Comparison of Model Predictions With Experimental Data for Different Number of Layers of Fiber Preform

The experimental data clearly demonstrated that, as the thickness of the structural layer increases, the length of the flow front and the lag time between the top and bottom of the mold increases significantly. This has important consequences for the manufacture of large parts by VARTM in which a number of injection lines are used in sequence to fill sections of the part. Each line is activated when the resin flow reaches it. Therefore, if the resin at the bottom layer lags behind the flow at the top layer, the injection line will get activated prematurely, since the section of the fiber preform lying below the injection line is not wetted out. If the lag is large for thick parts, as the experiments demonstrate, there may be formation of dry spots or areas that are not fully wetted out because the resin races ahead in the top layer. To avoid this problem, the injection lines in the sequential injection of large parts have to be spaced in an optimal manner. Since the bottom layer of the preform cannot be viewed, it is necessary to use a sensor-based control strategy to ensure that each injection line is activated only when the flow front reaches the bottom layer immediately below the line. These results are also significant because they demonstrate that the closure of inlets based on surface flow monitoring may result in significant dry-spot formation and make a strong case for on-line sensing, control, and optimization of the VARTM process.

3. CONTROLLED ATMOSPHERIC PRESSURE RESIN INFUSION.

CAPRI [24] (see figure 18), patented by The Boeing Company, is a VARTM variant that was developed to improve thickness/fiber volume variability in infused composites. Characteristic

points are preinfusion debulking (repeated compression-relaxation of preform), application of partial vacuum to the resin reservoir during infusion, and lowering the pressure gradient from inlet to vent location. This results in a smaller thickness gradient, but it can increase the infusion time significantly.

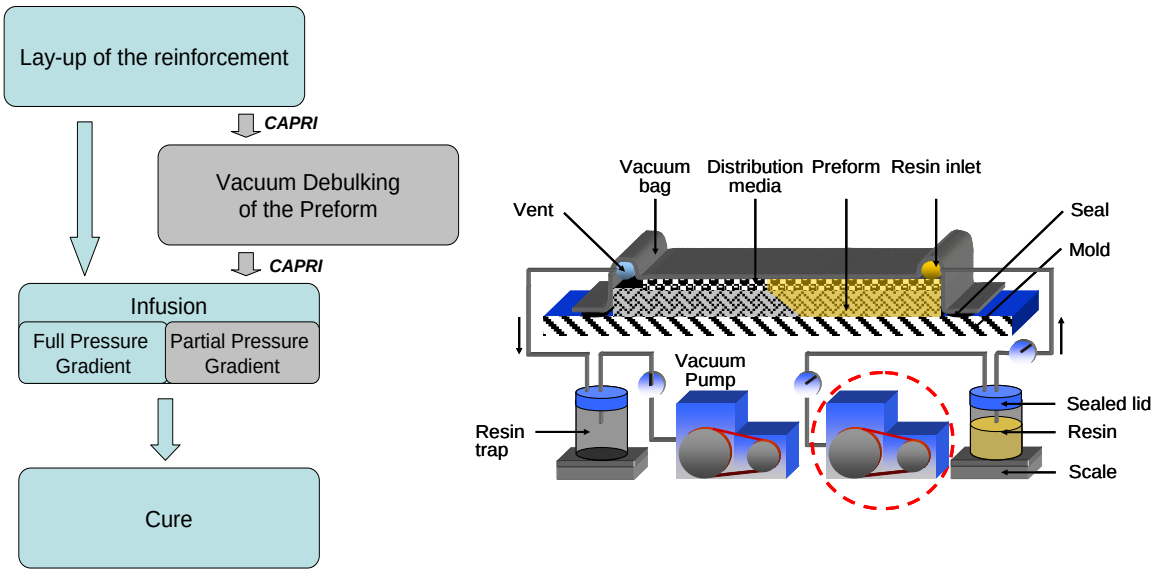

Figure 18. The CAPRI Setup and Processing Steps

The compaction behavior of the preform [25 and 26] is an important VARTM parameter that impacts both the infusion process as well as the final part thickness. The CAPRI process changes the compaction and permeability behavior during the debulking process prior to infusion. Figure 19 shows an out-of-plane permeability cell [27], which can characterize the permeability and compaction changes during dry debulking. The system is using 1D Darcy flow to equate the permeability based on the measurement of the flow rate and pressure drop across the reinforcement. The system is placed under a mechanical loading machine allowing controlled cycling of the pressure to simulate a typical vacuum debulking step during CAPRI processing. Slight system modification allows in-plane and out-of-plane permeability measurement with both gaseous and fluid flows.

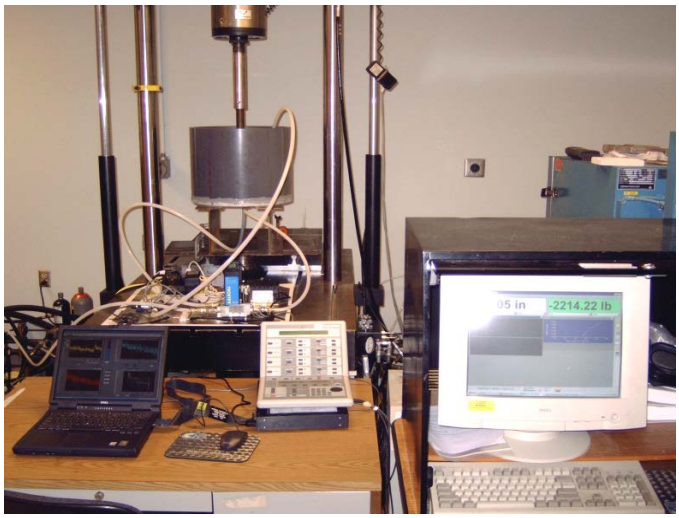

Figure 19. Out-of-Plane Air Permeability Cell Setup

The permeability changes during debulking of a 15-layer fabric stack (24-oz plain weave E-Glass 324-2407 supplied by Mahogany Company of Mays Landing, Inc.) was characterized using the permeability cell. Figure 20 shows the reduction in permeability for each debulking cycle under maximum load (100 kPa). The figure shows that the greatest reduction occurs during the initial debulking cycles. After 200 cycles, the permeability drops to approximately 20% of the undebulked baseline material, potentially increasing the infusion time and lead length during part impregnation.

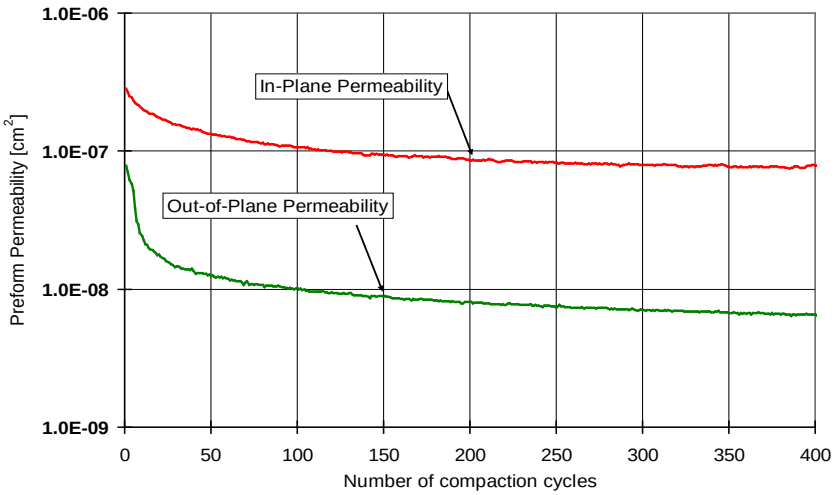

Figure 20. Permeability as a Function of Debulking Cycle

Figure 21(a) compares the dry compaction behavior before and after 400 debulking cycles, and figure 21(b) shows the thickness reduction during the first 400 debulking cycles. During each debulking cycle, the compaction pressure was increased to 90 kPa in 30 seconds and decreased to approximately 15 kPa in 30 seconds. The result of the nesting effect on thickness can be clearly observed. A thickness reduction of approximately 0.4 mm for the same compaction pressure

before and after 400 debulking cycles corresponds to an approximately 5% decrease in total thickness or 5% increase in fiber volume fraction. The maximum thickness difference from the uncompacted (15-kPa) to the compacted (80-kPa) preform changes from 0.4 mm for the undebulked case to 0.25 mm for the debulked case, indicating a reduced springback effect of the preform. The thickness is primarily reduced during the initial debulking cycles, as shown in figure 21(b). The first 100 cycles reduce the fiber preform thickness by 0.3-mm versus an additional 0.1-mm reduction for the remaining 300 cycles. The overall thickness reduction will increase the average fiber volume fraction in a VARTM part, and the reduced springback effect of the uncompacted versus compacted preform could potentially reduce the thickness gradient of the preform during infusion, improving dimensional tolerances.

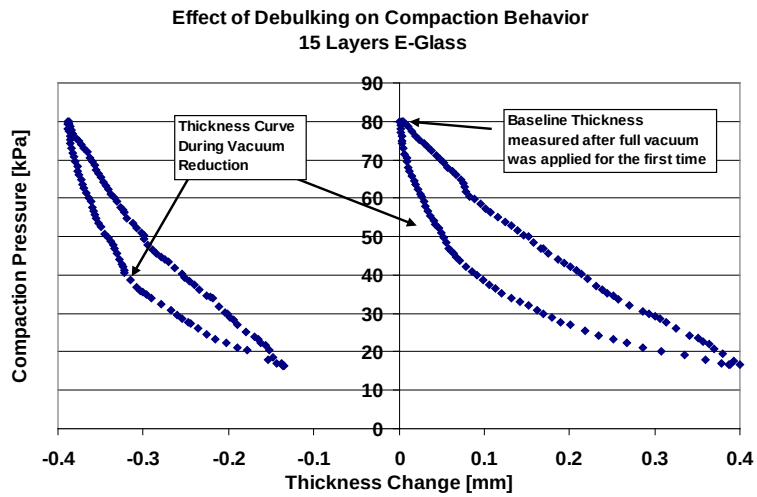

(a)

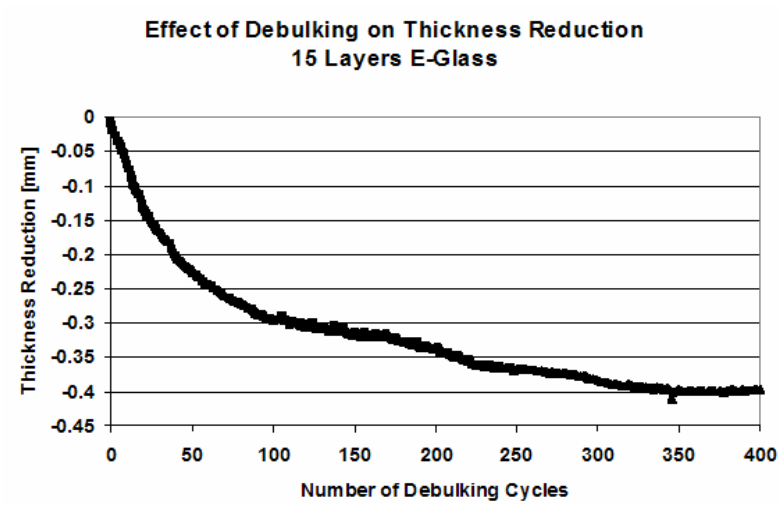

(b)

Figure 21. Compaction Behavior (a) Before and After 400 Debulking Cycles, and (b) Thickness Change at Each Debulking Cycle Measured During Peak Vacuum

The CAPRI process incorporates the debulking step to increase the overall fiber volume fraction prior to infusion. Another effect of the debulking step is the overall springback reduction, which decreases the thickness difference between fully and partially compacted preform. The CAPRI process further decreases the thickness gradient by reducing the pressure in the infusion bucket below 100 kPa, ensuring that the infused preform is at least partially compacted with the minimum compaction pressure of the infusion bucket.

Infusion experiments were conducted to evaluate the effect of debulking and partial pressure gradient on thickness, pressure, and infusion time development. All experiments used a 60- by 10-cm preform with 15 layers of 24-oz plain weave E-glass (324-2407 supplied by Mahogany Company of Mays Landing, Inc.), as characterized in the previous section, and corn syrup with an approximate viscosity of 0.17 Pa·s. Four VARTM scenarios were evaluated:

1. The Full-Vacuum scenario maintained a 100-kPa pressure gradient between the injection and vent bucket by applying full vacuum in the vent bucket and no vacuum in the resin container. The preform was not debulked prior to infusion.

2. The Full-Vacuum Debulked scenario added the debulking step to the first scenario.

3. The Half-Vacuum scenario applied partial vacuum pressure (50-kPa) to the infusion bucket and the fabric was not debulked prior to infusion.

4. The Half-Vacuum Debulked scenario combined scenarios 2 and 3, implementing the full CAPRI process.

Figure 22 shows the experimental station to measure the thickness development during infusion. The setup uses a mold with four integrated pressure sensors and a CCD camera to determine the bottom and top flow as well as the pressure gradient along the flow path. Four linear variable differential transformers placed on top of the bag and at the location of the tool-mounted sensors were used to measure the thickness change during vacuum debulking and infusion.

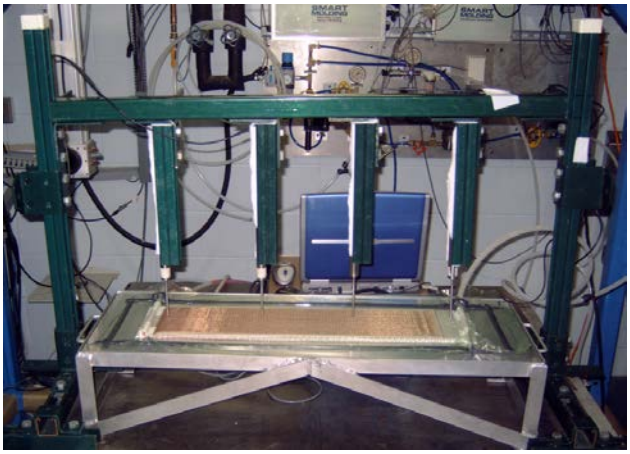

Figure 22. Setup to Determine Infusion and Dimensional Tolerance Parameters

Figure 23(a) shows the pressure change of the first mold-mounted sensor near the infusion port during resin injection. As anticipated, the pressure rapidly reduced for all four scenarios when the resin reached the sensor due to the pressure gradient between the resin bucket and flow front location. Nevertheless, the half-vacuum cases allowed a reduced pressure drop in the preform to about 60 kPa, whereas the pressure of the open resin bucket scenarios reduced to approximately 20 kPa. The injection bucket was placed on the manufacturing floor approximately 1 m below the mold to ensure compaction of the bag near the infusion gate. This explains the differences of the injection gate pressure level compared to the bucket pressure due to the gravitational pressure drop in the injection tubing. The final pressure gradient after full infusion is shown in figure 23(b). The larger pressure gradient between the injection and vent gates is shown for the open bucket cases. The vent gate pressure was approximately 97 kPa for all cases, showing that there is only minimal pressure drop in the vent tubing.

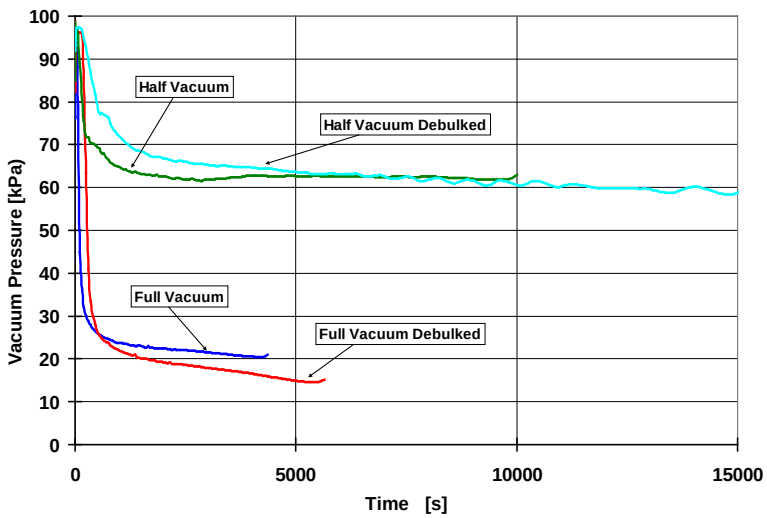

(a)

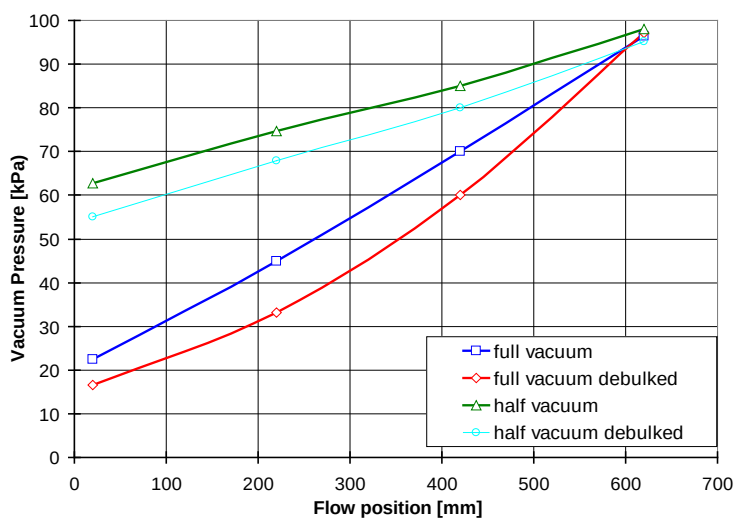

(b)

Figure 23. Preform Pressure During Resin Infusion: (a) Development Near the Infusion Port During Injection and (b) Final Pressure Gradient After Full Infusion

The pressure gradient in the preform developed during infusion dynamically changed the thickness of the preform in the flow region. Figure 24 shows the final thickness gradient for all four scenarios after complete wet-out. As shown, the thickness near the vent location (at the 60-cm mark) is approximately 8.2 and 7.8 mm for the undebulked and debulked cases, respectively. The vent location thickness is not influenced by the variable pressure applied in the infusion bucket due to the constant full vacuum applied in the vent bucket. For the debulked case, only a small difference in the thickness gradient can be observed. This may be due to the reduced springback behavior of the debulked fabric and the half-vacuum pressure applied at the injection gate even for the open resin bucket case. The thickness gradient is increased in the undebulked case, reflecting the larger springback potential of the preform. In addition, the thickness at the injection line for the baseline scenario 1 (full vacuum) is larger (approximately 8.48 cm) compared to the infusion with the reduced pressure gradient (approximately 8.33 cm), reducing the thickness gradient from 3% to 1% of total preform thickness from scenario 1 to scenario 2. The additional debulking step further reduced the gradient to less than 1%.

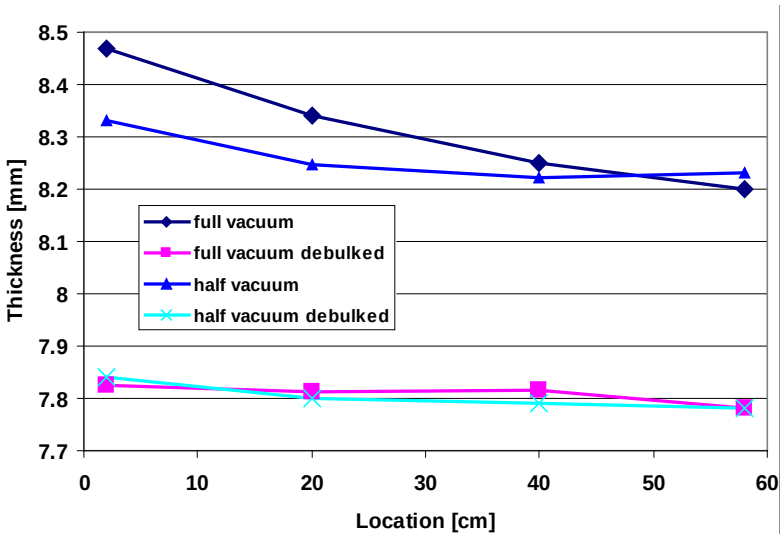

Figure 24. Final Thickness Gradient After Full Infusion

The infusion behavior was also greatly affected by the different infusion scenarios. The debulking decreased the permeability in both in-plane and out-of-plane directions by approximately 80%, thus increasing the required fill time. In addition, applying a partial vacuum on the injection line reduced the pressure differential between the vent and injection gate and, thus, increased the infusion times as well. The use of the metallic distribution media ensured that the compaction behavior of the distribution media was negligible. A separate flow experiment confirmed that the permeability of the debulked and undebulked distribution media was only slightly reduced (see table 3).

Figure 25(a) shows the surface filling time measured by a CCD camera, and figure 25(b) shows the tool-side flow time measured by four tool-mounted flow sensors. It is observed that the flow times were increasing from scenarios 1 through 4, as anticipated. The partial vacuum applied to the preform increased the fill time by approximately three times, whereas the decrease in preform permeability changed the fill time by less than 40%.

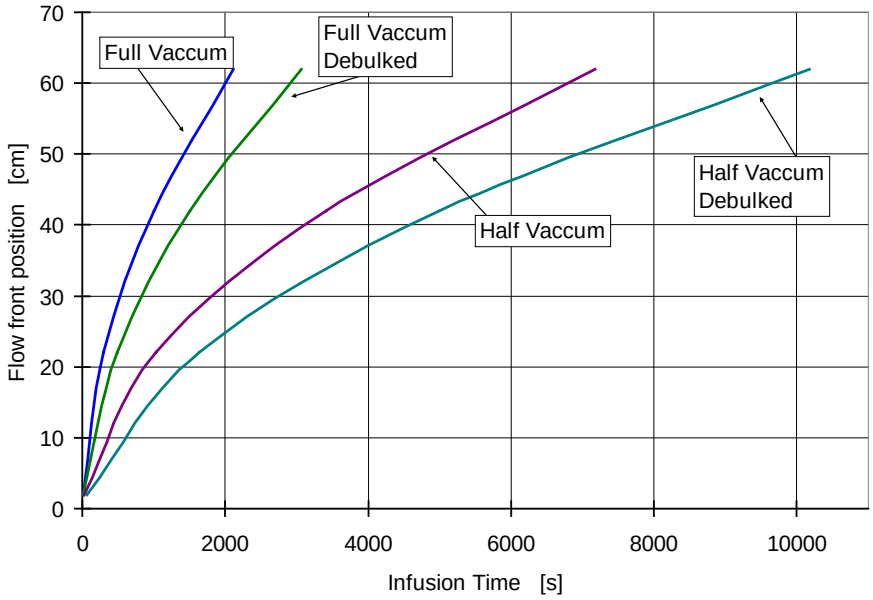

(a)

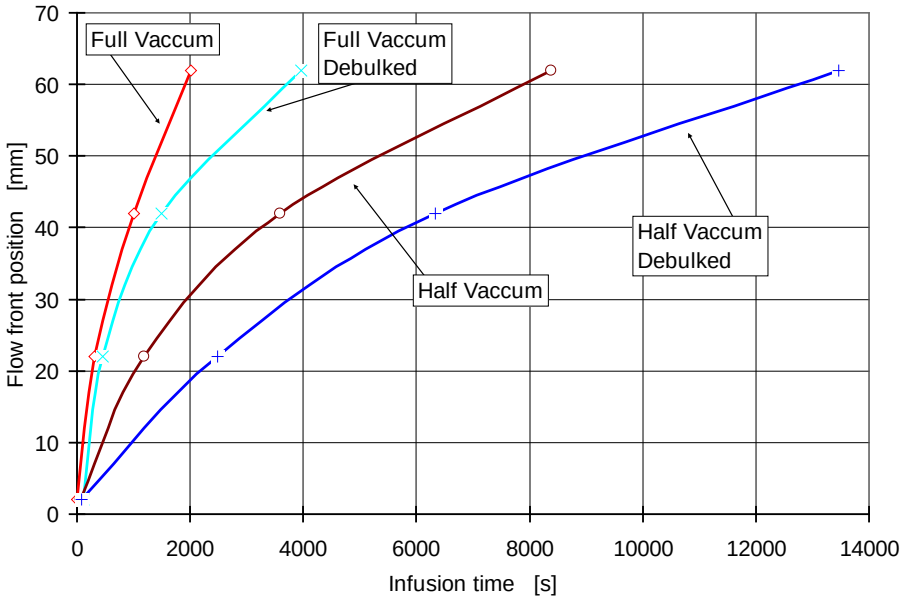

(b)

Figure 25. Flow Profile: (a) Surface and (b) Tool Side

The analytical models described in section 2 take into account the material parameters to predict the flow times and through-the-thickness profile during infusion. The through-the-thickness flow profile during VARTM processing is often defined by the lead length, which corresponds to the distance between the surface and tool resin flow front position. The lead length is an important characteristic because it determines the timing of the opening and closing of sequential injection lines during large-scale infusion, as outlined in section 3. The lead length is greatly influenced by the through-the-thickness permeability, and thus, it is expected that the reduction of the

out-of-plane permeability during debulking increases the lead length. The analytical model was used to compare the experimentally obtained lead length with the model prediction. Table 4 summarizes the model input, which was obtained from the independent material property measurements. The initial in-plane permeability K_{1xx} and out-of-plane permeability, K_{1yy}, were obtained from the permeability tests shown in figure 3. The in-plane permeability of the distribution media, K_{2xx}, with and without debulking was obtained similarly.

Table 4. Input Properties for the Analytical VARTM Model

	Full Vacuum	Full Vacuum Debulked	Half Vacuum	Half Vacuum Debulked
K_{1xx} (cm^2)	1.00E-05	8.00E-06	1.00E-05	8.00E-06
K_{2yy} (cm^2)	4.65E-07	8.05E-08	4.65E-07	8.05E-08
K_{2xx} (cm^2)	6.24E-08	6.52E-09	6.24E-08	6.52E-09
h_1 (cm)	0.05	0.05	0.05	0.05
h_2 (cm)	0.82	0.78	0.82	0.78
Porosity 1	0.45	0.45	0.45	0.45
Porosity 2	0.75	0.75	0.75	0.75
Viscosity (Pa·s)	0.17	0.17	0.17	0.17
Pressure (Pa)	85,000	85,000	35,000	35,000
Length (cm)	42	42	42	42

Figure 26(a) shows the lead length measured by the average differences of the flow position of the surface and tool flow when the tool-mounted sensors were activated at the 22- and 42-cm locations, and it shows a comparison to the model prediction. These measurement points ensure a fully developed flow profile while still allowing continuing surface flow. It is shown that the lead length increases by more than 200% for the debulked cases mainly due to the reduction in out-of-plane preform permeability. The experimentally obtained half-vacuum cases slightly increase the lead length (from 43 to 56 mm and from 102 to 122 mm for the undebulked and debulked cases, respectively). This may reflect an average decrease of the permeability due to the increased compaction in the flow region that is not captured in the flow model or model inputs. Overall, good agreement of the experimental and modeled lead lengths can be observed. The infusion times were predicted accurately for the full-vacuum infusion case, but the simulated half-vacuum infusion times are underpredicted compared to the experimental results. This could be due to the discrepancy of the independently measured permeabilities with the flow experiment resulting in extended flow times, as well as the influence of the half-vacuum pressure on overall compaction and permeability. Nevertheless, the model does accurately predict the trend of increase in flow times. Further study is required to isolate the origin of the discrepancy.

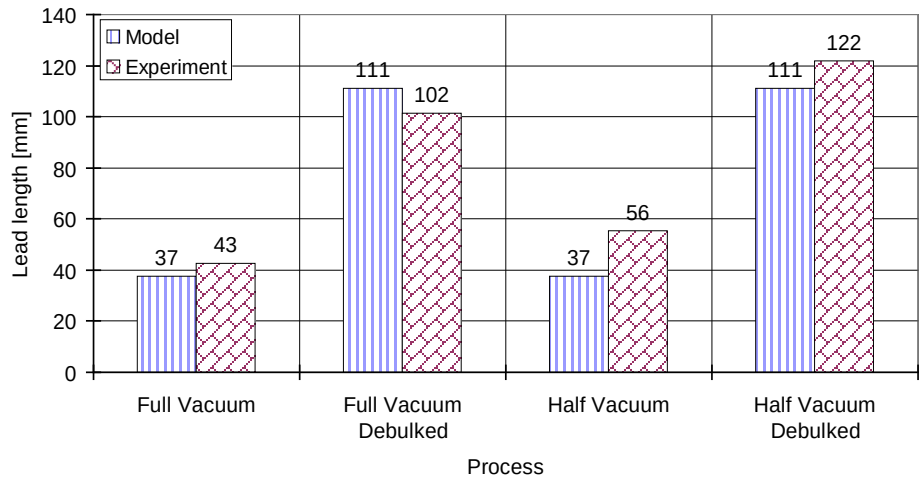

(a)

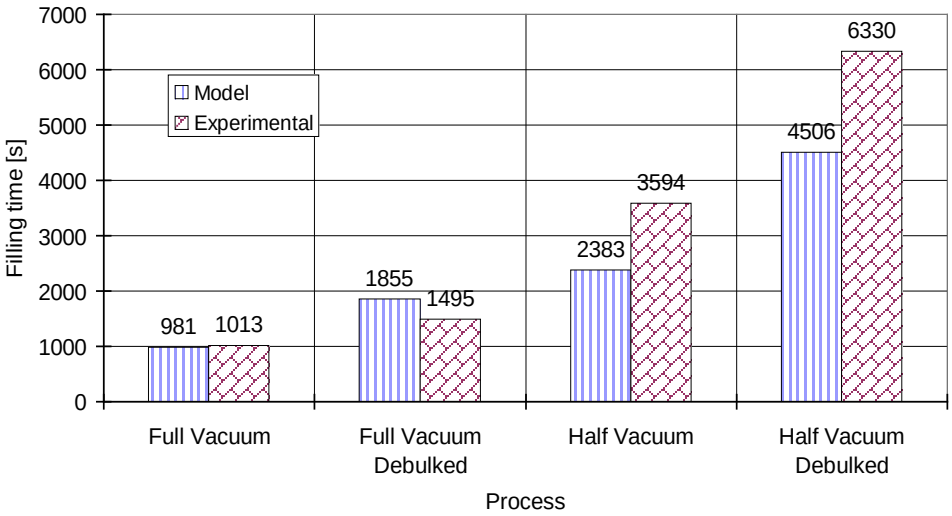

(b)

Figure 26. (a) Comparison of Experimentally Obtained Lead Length and (b) Infusion Times

The study showed that the infusion behavior was greatly influenced by these CAPRI process variations. The debulking process reduced the permeability of both the in-plane and out-of-plane directions and, thus, increased flow time and lead length during infusion. The vacuum pressure applied in the injection bucket reduced the pressure differential and increased total filling time.

Nevertheless, the benefit of the process is a substantial increase in fiber volume fraction during debulking. In the case of the 24-oz plain weave E-glass fabric, a 5% increase in total compaction and fiber volume fraction was observed after 400 debulking cycles. In addition, debulking also reduced the overall springback effect by almost 40%, thus reducing any potential thickness gradient during VARTM processing. The application of a partial vacuum in the injection bucket can further reduce the thickness gradients observed during infusion, which is particularly important for preforms with large springback. In the 24-oz fabric case, the reduced thickness gradient can be observed for the undebulked preform but is negligible for the debulked preform.

Overall, the CAPRI process produced more uniform thickness components with higher fiber volume fraction, and thus, came closer to the quality and performance of autoclave parts. The tradeoff is the reduced permeability increasing the infusion time and lead length, which could provide more challenging processing, particularly for thick sections or low-permeability parts. In addition, the debulking step and additional vacuum applied to the injection bucket adds to the hardware requirement and cycle time of the setup.

4. VACUUM-ASSISTED PROCESS.

The VAP uses an additional membrane material below the vacuum bag. The membrane is permeable to gas and impermeable to the resin at typical VARTM pressure and can be used at temperatures up to 200°C. During the infusion, the resin cannot penetrate through the membrane resulting in uniform vacuum on the surface. The membrane provides continuous resin degassing during infusion and staging. The need for rebagging to place a new breather cloth to ensure excellent vacuum during cure is eliminated. Also, the vent line is placed between the bag and membrane, minimizing the potential for resin bleeding. This setup reduces the thickness gradient and decreases the void content in the final part.

Figure 27 shows a typical VAP setup. The injection line, distribution media, and preforms are sealed inside the membrane. The breather material covers the entire membrane to ensure uniform vacuum distribution on the part. The vent is located on top of the breather material. The vacuum bag seals all these materials. The peel ply was laid on top of the preform and under the distribution media. The membrane seals the complete part, including the injection line, but not the vent. Finally, the breather cloth and vent line are laid up, and the bag seals the membrane and fabric stack.

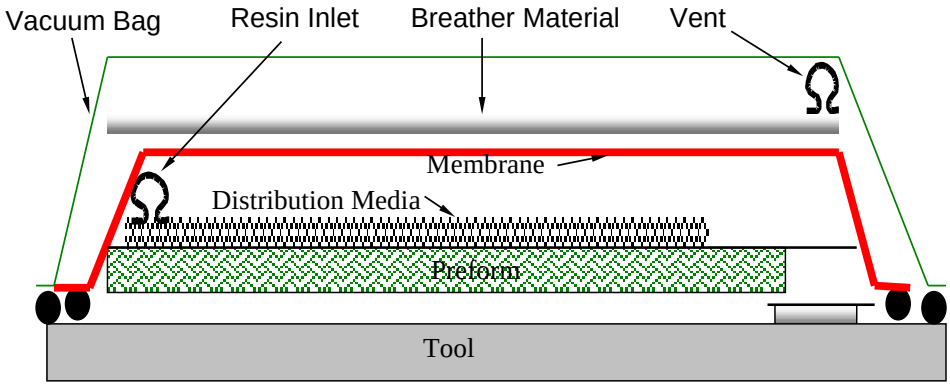

Figure 27. The VAP Setup (The vent is located between the membrane and vacuum bag, allowing continuous resin degassing.)

VAP requires additional labor to seal the membrane and for egress of the injection line through the bag and membrane. Additional material costs are incurred for the membrane and breather cloth. The infusion process can be visually observed on the surface during a traditional SCRIMP process. This benefit is lost in the VAP process since the membrane is not transparent. However, advancements in flow and cure sensing for automation and control of the VARTM

process overcome this potential disadvantage. Special care has to be taken while sealing the membrane. Excessive stretching of the membrane used in this study resulted in a membrane leak, allowing resin to penetrate the material. A more robust membrane has since been developed by W. L. Gore & Associates, Inc. and tested successfully at EADS.

Experiments were conducted to compare parts fabricated with the VAP and SCRIMP process. Preforms (80-cm-long by 20-cm-wide by 0.84-cm-thick) consisting of 15 layers of 24-oz woven E-glass (plain weave) were injected with Applied Poleramics, Inc. SC-15 epoxy resin (viscosity approximately 350 megapascal (mPa) at 25°C). The permeability of the preform was independently measured to be 3.63 x 10^{7}cm^{-2} in both in-plane directions and 7.00 x 10^{-5}cm^{2} in the out-of-plane direction. The experiments evaluated flow characteristics, mechanical properties, and robustness of the infusion process to minimize dry-spot formation.

4.1 INFUSION CHARACTERISTICS OF THE VAP AND SCRIMP PROCESS.

The flow behavior of the SCRIMP and VAP process were compared by monitoring the arrival time of the resin in-plane and through the thickness at the tool surface. During the VAP infusion, the flow front on the surface of the preform could not be observed visually due to the membrane. Here, a SmartWeave sensor system was used to detect the surface flow front. A sensor was embedded between the top layer of the fabric and distribution media every 5 cm. The tool-side flow was obtained by a digital CCD camera through a glass tool.

Figure 28 shows the experimental results of the resin arrival times on both the surface and tool side. The first 70 cm were monitored to minimize any end effects due to the start of the preform, and the breather cloth was laid under the fabric. In addition to the experimental results, the analytical model introduced in section 2 was used to predict the arrival time for the fabric-resin combination during SCRIMP processing. The model inputs are listed in table 5.

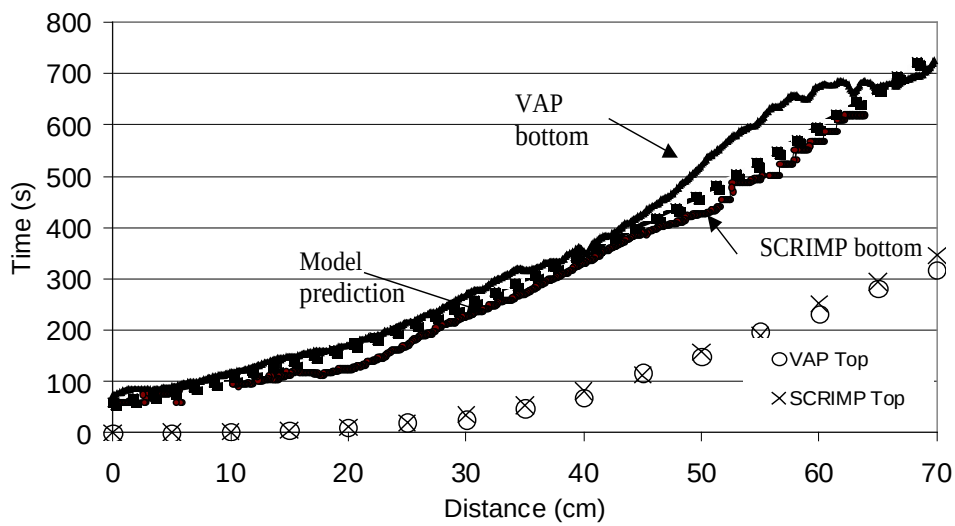

Figure 28. Surface and Tool-Side Flow Front Comparison of the VAP and SCRIMP Processes

Table 5. Parameters for Flow Model

Permeability of Preform at 56% F_v (in-plane) (cm^2) [28]	Permeability of Preform at 56% F_v (out-of-plane) (cm^2) [28]	Permeability of Distribution Media at 10% F_v (cm^2) [28]	Preform Thickness (cm)	Preform Length (cm)	Viscosity (mPa)
3.63×10^{-7}	9.20×10^{-9}	7.00×10^{-5}	0.84	80	350

F_v = Fiber volume fraction

The resin flow on the surface is mainly governed by the permeability of the distribution media. It is similar for both the VAP and SCRIMP processes. The arrival time on the tool is determined by the preform thickness and through-the-thickness permeability of the fabric. The model predicts the arrival time on the tool and the nonsaturated lead length to be approximately 37 cm. Good agreement is shown for both experimental setup and model prediction. The lead length for both processes is approximately 33 cm and constant, which is calculated by comparing the arrival distances on the surface and tool side. Overall, the VAP process seems to exhibit similar flow behavior compared to the VARTM infusion. The arrival times on the top surface are dominated by the high permeability of the distribution media, and little difference is noted between the two processes. However, the arrival times on the tool surface are consistently higher for VAP versus SCRIMP. One possible explanation is that VAP maintains a constant level of preform compaction during infusion since a uniform vacuum is applied across the entire panel via the membrane. In contrast, a pressure gradient develops during SCRIMP that allows springback of the fabric stack. Higher preform compaction is known to reduce preform permeability. Consequently, the slightly higher compaction achieved in VAP led to the reduced velocity and higher arrival times.

The amount of infused resin weight (weight loss of the injection bucket) and resin bleeding (weight gain of the vent bucket) was recorded as a function of time using two high-precision electronic scales (see figure 29). During the SCRIMP process, the flow rate decreases until the part is filled. At this point ($t \approx 1100$ s), the resin is pulled out of the part and fills the tubing to the vent bucket. The weight loss remains constant, versus time and the resin-bleeding phenomena fills the bucket with the same flow rate. This process ensures a maximum resin weight injected into the dry preform. However, no resin bleeding was found in the VAP process because the vent is separated from the preform by the membrane. Initially, the flow rate decreases until the part is filled. Interestingly, the resin net gain into the part continues at a lower but constant flow rate unless the inlet is closed, which results in an increase in the total resin amount infused into the dry preform. It was concluded that a continuous resin infusion in VAP can lead to thicker parts and lower fiber volume fraction (that are uniform throughout the part due to the membrane). To maximize the fiber volume fraction, the infusion has to be stopped when the preform is fully wetted out, requiring either sensors to detect the resin arrival at the end of the preform or infusion of a calculated amount of resin to achieve optimum fiber volume fraction without voids.

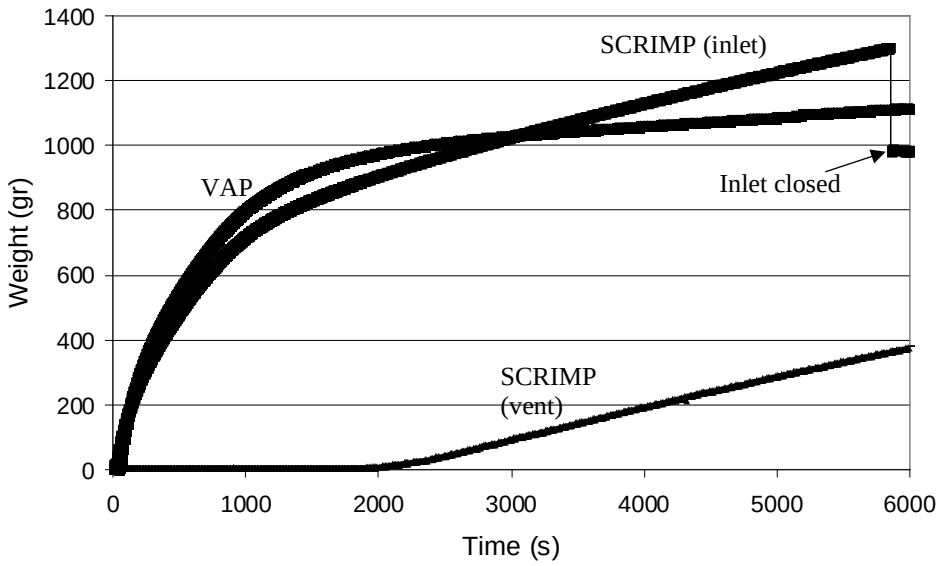

Figure 29. Infused Resin Weight as a Function of Time

A potential drawback of any liquid molding process is the expertise needed to obtain optimum locations for the injection lines and vents. The infusion will either take too long if the injection lines are not placed correctly or dry spots will develop if the vents are not in the same location as the last fill. In addition, the inherent variability of the material (e.g., permeability of the preform and distribution media, resin viscosity.) and lay-up and bagging procedures (e.g., placement of distribution media and inlets, racetracking around perimeter) can significantly impact the flow patterns, location of last fill, and the development of dry spots due to the fixed position of the vents. Improved process robustness would result in less scrap and lower costs. In the VAP process, only one vent is needed, and it can be placed at any location on the membrane, which results in a uniform vacuum on the infusion surface.

The experimental setup in figure 30 was designed to show the robustness of VAP by selecting an example that would intentionally create dry spots in the SCRIMP process. An L-shaped cutout was taken from the preform and tacky tape was used to separate the fabric parts. The remaining preform (25.4 cm long by 7.6 cm wide) was left without a distribution media, and the infusion was started from the left (injection line) toward the vent on the right. In both processes, the resin flowed uniformly along the distribution media until it reached the cutout without the high-permeability layer. SmartWeave sensors were applied every 2.5 cm to evaluate the wet-out on the surface, and a CCD camera monitored the tool flow.

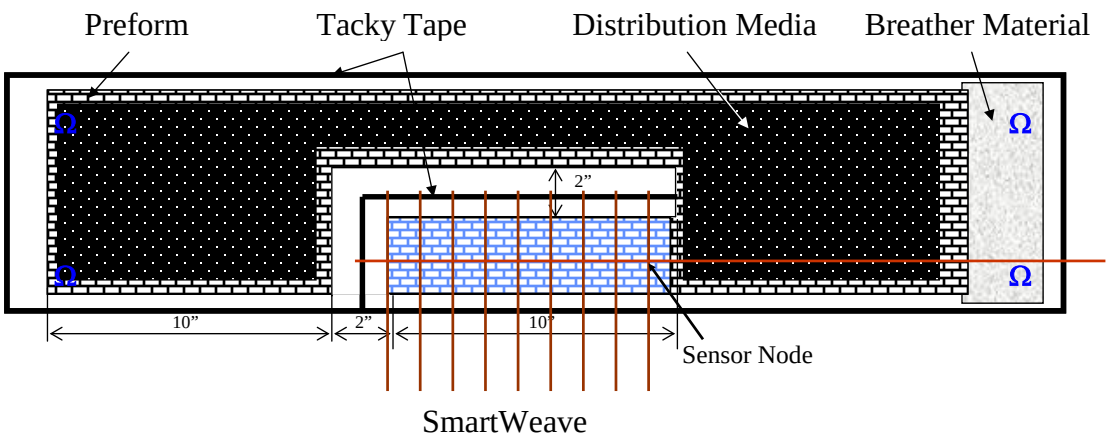

Figure 30. The Process Robustness Experiment

Figure 31 shows the resin arrival time as a function of cutout location. The arrival time was zeroed when the first sensor node on the surface was wetted out. For both processes, the flow speed was greatly reduced because no distribution media was used in the cutout area. The SCRIMP process resulted in large dry-spot development both on the surface and on the tool side. Approximately 12.5 cm on the bottom and 7.5 cm on the surface were not wetted out. The dry spot is isolated from the vacuum: VAP results in a robust process when dry-spot development is minimized by the resin that is now flowing from the inlet directly into the vent. In this example, continuous recirculation of resin did not enable the dry spot to be filled.

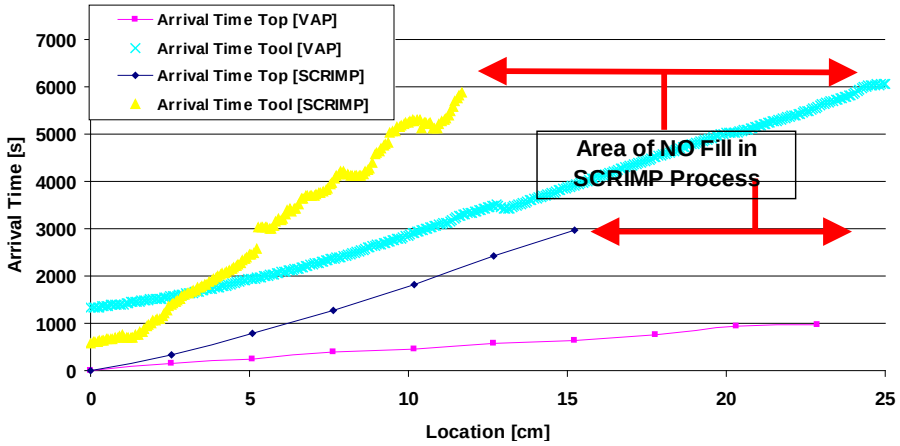

Figure 31. Arrival Time of VAP and SCRIMP Injection on Separated L-Part

On the other hand, the VAP process allowed a continuous application of vacuum through the membrane throughout the panel. In this example, vacuum was always applied to the region of the last fill and allowed for a slow, but complete, fill of the fabric. After approximately 6000 seconds, the cutout area was filled, and the infusion was stopped. This example illustrates the improved robustness of the VAP process, showing that the correct placement of the vent location is not critical to the successful infusion of the preform. In summary, the VAP exhibited similar flow characteristics compared to VARTM parts but with increased robustness to the selection of

vent placement. The separation of the preform from the vent by the membrane allowed uniform vacuum and continued infusion, even after a complete fill, minimizing further resin waste. Section 4.2 evaluates the material and mechanical properties of the VAP parts and compares them to the SCRIMP-processed parts.

4.2 MATERIAL PROPERTIES EVALUATION.

4.2.1 Thickness Development.

The part thickness is changing dynamically throughout the liquid molding process. Initially, vacuum debulking steps can be applied to increase dry-preform compaction. During SCRIMP infusion, a pressure gradient develops in the area wetted with resin due to flow that causes changes in compaction (i.e., thickness) as a function of time and location. After infusion, closing the injection line enables full and uniform vacuum pressure to be reestablished. If the resin has not gelled during this stage of the process, this can lead to increased compaction and uniformity of the final part thickness and properties. If the resin gels, gradients will be frozen into the part. The optimum process conditions are dependent on the resin properties. The VAP process provides uniform vacuum throughout the process, therefore the process conditions will be more universally applicable to a wide range of resin systems.

A laser-scanning system was used to monitor the thickness of the preform throughout the infusion and curing process. The data were saved, and a data reduction was applied to evaluate the thickness distribution after infusion of the final part. Figure 32 shows a comparison of the thickness change of the VAP and SCRIMP parts. The baseline was taken before infusion of the resin; thus, the data illustrate the change in thickness due to the springback effect during infusion and cure. The infusion line pressure was approximately 1 atmosphere (open bucket), whereas the vent was under full-vacuum. During SCRIMP processing, the resin separated the vent and injection line and a 1-atmosphere pressure gradient developed throughout the part. The preform compaction was related to the applied pressure, resulting in the observed thickness gradient. For the 24-oz woven fabric, the thickness near the infusion line increased by approximately 5% (0.06 cm of a total thickness of 0.84 cm). After a complete fill, the infusion line was closed, resulting in a gradual recovery of full vacuum throughout the part. This process can take several hours (the gel time of SC-15 epoxy resin is greater than 10 hours at room temperature) and depends on the resin viscosity, permeabilities, and part dimensions. After several hours, the thickness gradient was negligible. Furthermore, an overall reduction in thickness was observed due to the continuous resin bleeding that was a direct result of the increased compaction in the part.

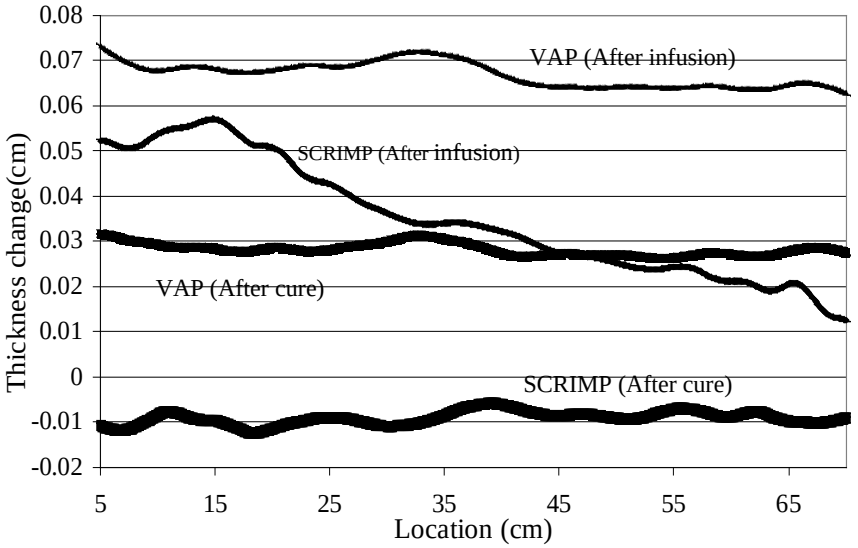

Figure 32. Thickness Distribution After Infusion and Cure for Both VAP and SCRIMP

During VAP processing, the membrane maintained a uniform vacuum (i.e., minimal pressure gradient) on the part surface that resulted in a much smaller thickness gradient after infusion. The gradient was approximately 0.014 cm over the part length after infusion, representing a 77% reduction compared to the SCRIMP results. After full infusion of the part and prior to the gelation of the resin, the small gradient and total thickness was further reduced after closing the injection line. The injection line closing resulted in full-vacuum pressure in the preform, further increasing compaction and impregnation of the fiber tows and promoted redistribution of the resin from the inlet to the vent. During SCRIMP processing, bleeding out of the vent occurred until gelation, which resulted in a lower average thickness and a thickness gradient reduction. The final thickness of the VAP part after cure was significantly higher than the SCRIMP panel due to the injection of excess resin (see figure 32) during infusion (i.e., inlet may not have been closed at the optimal time) and the lack of resin bleeding in the process. The overall thickness of the VAP panel was approximately 9% greater than the SCRIMP panel in this comparison. Clearly, the VAP process had the potential to achieve the same level of compaction since full vacuum was applied in both processes. Additional studies on flow rate control are needed.

4.2.2 Void Content and Fiber Volume Fraction Evaluation.

The final thickness difference can be directly contributed to changes in the fiber volume fraction. Table 6 compares the fiber volume fraction measured in accordance with ASTM D3171-99 [29] and shows the void content (ASTM D2734-94) [30]. Ten samples for each tests were taken from SCRIMP and VAP panels to calculate the average and standard deviation.

Table 6. Fiber Volume Fraction and Void Content With and Without Degassing of Resin

	Fiber Volume Fraction (%)/ Standard Deviation (%)		Void Content (%)/ Standard Deviation (%)	
	No Degassing	Degassing	No Degassing	Degassing
VAP	50.9/0.5	52.8/0.7	0.37/0.3	0.23/0.2
VAP_{low}	54.0/0.3	n/a	0.6/0.3	n/a
SCRIMP	56.0/1.0	56.21/1.2	1.64/1.2	1.07/0.7

The fiber volume fraction of the SCRIMP panel reached approximately 56% with a standard deviation of 1.0%. For comparison purposes, two VAP panels are shown. The first panel was fabricated with the infusion bucket placed at the same height as the tool surface (VAP), whereas, the second panel was fabricated with a lowered bucket (≈1.3 m below the tool surface) (VAP_{low}). The VAP_{low} setup showed a reduction of total infused weight compared to the VAP setup, which resulted in a higher fiber volume fraction of 54%. The standard deviation for both panels was similar (0.5% for VAP setup and 0.3% for VAP_{low} setup), showing uniform panel quality. The VAP Panel had a lower fiber volume fraction with a 9% reduction of the SCRIMP baseline, which was directly attributed to the 9% thickness increase in the final part due to the excessive fill.

The void content was measured on several panels. Good manufacturing practice includes a degassing step of the resin before infusion to reduce the amount of air accumulated during mixing. The VAP process allows for continuing degassing of the resin, even after complete infusion. Volatiles generated during processing can escape through the membrane layer. None of the VAP specimens had more than 1% void content. The standard deviations for VAP panels with and without degassing the resin were constant, which showed the degassing effect of the membrane. The SCRIMP part without degassing had a void content of 1.64% ±1.2%, which was reduced to 1.07% ±0.7% by the degassing step. The VAP panels showed a large reduction of void content compared to autoclave process levels.

Overall, comparable fiber volume fractions can be achieved with VAP, but control of injected resin weight is needed. However, the VAP process results in a more uniform fiber volume fraction and void content within the panel. Autoclave levels of void content to meet aerospace requirements (V_c <1%) have been achieved with the VAP process.

4.2.3 Mechanical Test Evaluation.

Short-beam shear tests (ASTM D2344 [31]) were conducted on both VAP- and SCRIMP-processed panels. Figure 33 shows the test results for a VAP and SCRIMP panel using the degassing step with 52% and 56% average fiber volume fraction. Given the slight difference in fiber volume fraction, the short-beam shear strength of the VAP panel (44.2 mPa) is comparable to the SCRIMP panel (41.2 mPa). In addition, the VAP part shows improved repeatability by having a lower coefficient of variation (CV) of 3.8% compared to 4.5% CV of the SCRIMP part. Optimizing the fiber volume fraction during VAP processing would likely result in further improvement of the mechanical properties.

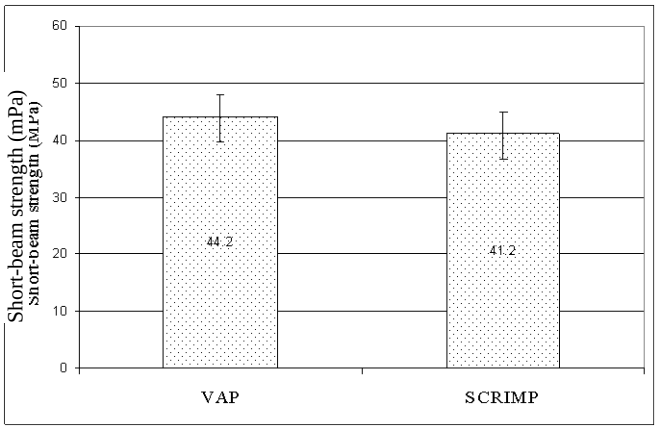

Figure 33. Short-Beam Strength Test Results

The results of the study showed that the placement of the vent location is not critical in VAP processing compared to SCRIMP processing for complete resin fill. It implies that the VAP process is a more robust filling process that enables manufacturing composite parts with complex geometries and/or inserts with low risk of dry-spot formation. Optimizing the infused resin amount during VAP processing is critical to achieve high fiber volume fraction, because the membrane does not allow resin bleeding. Nevertheless, this feature minimizes the resin waste independent of the resin gel time, which is another advantage of the VAP process. Also, the uniform vacuum pressure (VAP) results in a uniform thicknesses after infusion. The thickness gradient developed during SCRIMP can be reduced by closing the injection line after infusion only (if gel time is long compared to the time required for redistribution). The VAP process allows continuous degassing during infusion and cure, resulting in reduced overall void content levels. Overall, VAP processing resulted in more uniform fiber volume fraction, void content, and mechanical properties enabling applications in areas previously reserved for high-cost, autoclave-processed parts. A summary of VAP benefits is shown in table 7.

Table 7. Summary of VAP Benefits

	SCRIMP	VAP
Vent location	Optimized for place of last fill	No optimization necessary
Compaction	Thickness gradient due to pressure gradient during infusion	Reduced thickness gradient
Void content	Above 1% with high standard deviation	Below 1% with reduced standard deviation
Fiber volume fraction	High F_v but with large standard deviation	Lower F_v with lower standard deviation, can be optimized if optimum resin weight is injected into preform
Mechanical properties	Lower Short-beam shear results due to increased V_f even at high F_v	Lower COV for short-beam strength results

COV = Coefficient of variance
F_v = Fiber volume fraction
$V_{\text{f ibers}}$ = Volume occupied by fibers

4.3 MEMBRANE MATERIAL CHARACTERIZATION.

Several companies have developed a suitable membrane material [28 and 32]. The membrane is designed to be impermeable to the resin system but permeable to gases. In general, the membranes have a nanoporous structure and rely on the capillary pressure to maintain the barrier characteristics for the fluids. The characteristics change with the resin material and pressures used in the VARTM method and, thus, have to be designed for a particular setup.

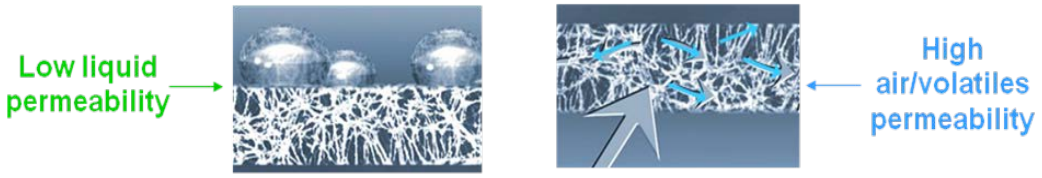

Figure 34. Low Resin Permeability Creates a Resin Barrier While High Air Permeability Enables Continuous Surface Venting During VAP Processing

The membrane initially used for the VAP by EADS was provided by W. L. Gore and Associates. It is manufactured in Germany under the commercial name Albatros. To better understand the membrane and its properties, W. L. Gore and Associates provided membranes with different pore sizes and thicknesses. Similar membranes were also provided by Donaldson, which belong to the Tetratex® family. Overall, the study involved three membranes from each provider: membrane W from W. L. Gore and Associates (W1 (the baseline), WA, and WB) and membrane D from Donaldson (D2, D1, and D4). All materials consisted of two layers: a 30- to 80-μm-thick membrane made of polytetrafluoroethylene (PTFE) and a support (carrier) layer. The structural support is used during handling and placed in the preform over complex geometries to retain integrity (limit stretching and tearing) during compaction and infusion during manufacture.

4.4 QUALITATIVE CHARACTERIZATION.

4.4.1 Optical Microscopy.

Figure 35 shows an optical micrograph of a cross-sectioned membrane that highlights the microstructure of both membrane layers. The material has a two-layer construction, in which the thinnest layer is the actual membrane and the thicker layer is its carrier. In fact, the membrane is a very thin material that is too fragile to be handled by itself without risk of distortion or tearing. Membrane thicknesses ranged from 30 to 80 μm.

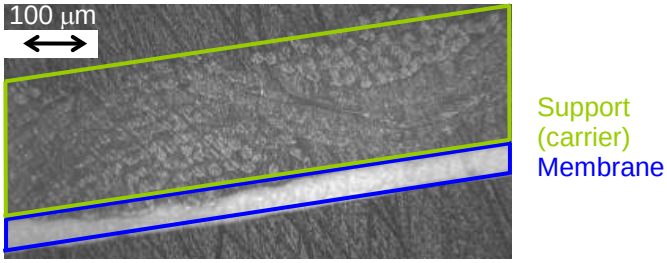

Figure 35. Scanning Electron Microscopy Image of the Cross Section of the Membrane

A scanning electron microscopy (SEM) provides higher magnification than an optical microscope and, thus, a more detailed image of the membrane. The SEM image (shown in figure 36(a)) shows the fibrous structure of membrane W1. Except for the large fibers, the fibers are randomly organized. Figure 36(b) shows a cross section of membrane W1, obtained by cryomicrotoming, which did not create a clear cut of the membranes. The second type of membrane is shown in figure 37. For this structure, the diameter of the fibers is approximately 250 nm.

Besides the structure of the membrane, the SEM reveals the carrier structure of the membrane W (see figure 38). In this case, it is a plain-weave structure made of polyethylene that will almost spontaneously be wetted by the resins. The support of membrane D is shown in figure 38. It is a nonwoven polyester support that will also spontaneously wet the fluids used in this study. Consequently, the PTFE layer provides the barrier properties to the nonwetting resins used in composite processing.

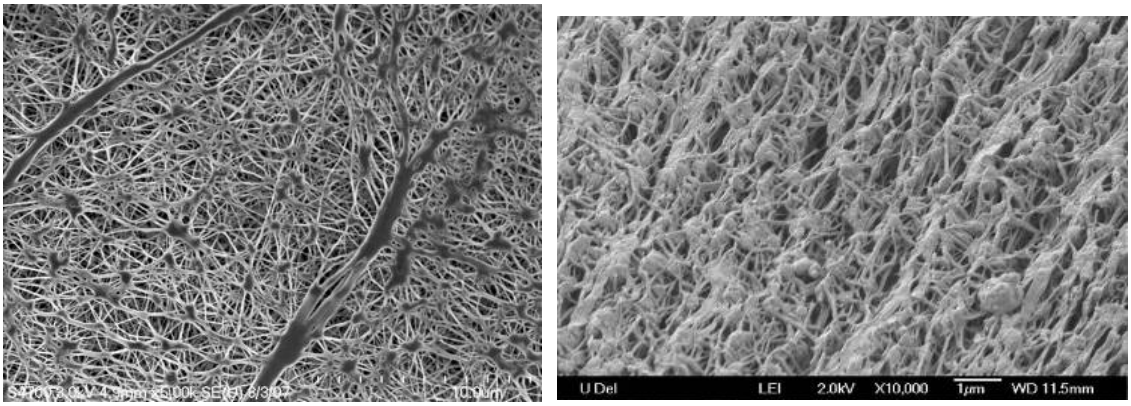

(a) (b)

Figure 36. (a) An SEM Image of Membrane W1 at 5000x Magnification and
(b) a Cross Section of Membrane W1 Cut by Cryomicrotoming

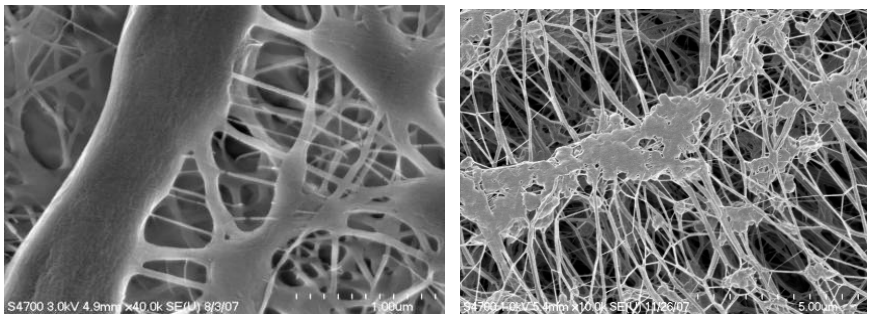

(a) (b)

Figure 37. (a) An SEM Image of Membrane W1 at 40,000x Magnification and (b) an SEM Image of Membrane D at 10,000x Magnification

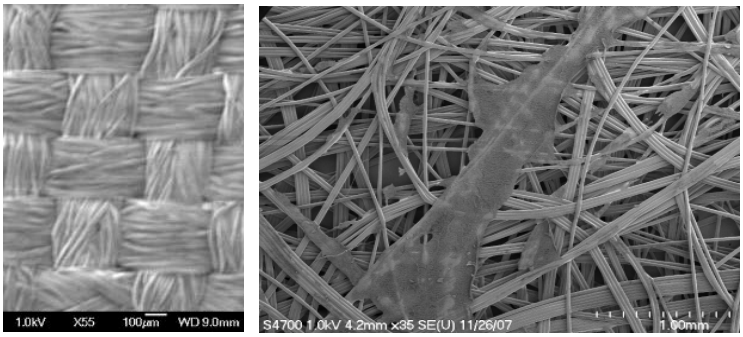

(a) (b)

Figure 38. (a) An SEM Image of Support W at 55x Magnification and (b) an SEM Image of the Donaldson Support at 35x Magnification

4.4.2 Membrane Thickness.

Cryomicrotoming combined with SEM was used to obtain a precise measurement of the thickness (figure 39) for membrane W1, which did not have any manufacturer data. For the other membranes, the manufacturer information was used. The membranes' thicknesses ranged from 30 to 80 micrometers (table 8). The membrane thickness, even for the thinnest membrane, was at least one order of magnitude higher than the mean pore size, confirming the assumption that the pores can be treated as capillary tubes.

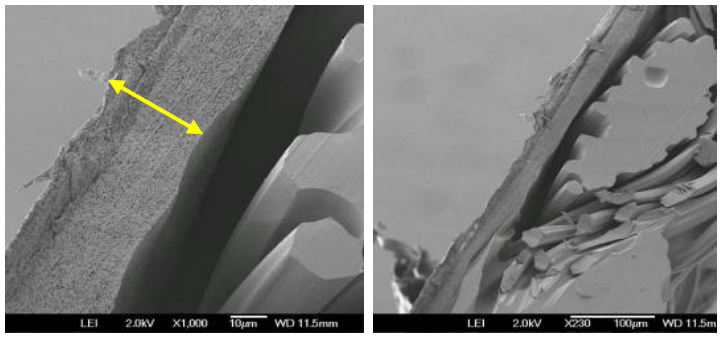

(a) (b)

Figure 39. (a) An SEM of the Membrane W1 Cut by Cryomicrotoming and (b) Close-Up

Table 8. Thickness of Membranes

Manufacturer	Name	Thickness (μm)	Source
W. L. Gore & Associates	W1	44 ±7	Cryomicrotoming
	WA	75 ±1	W. L. Gore and Associates GmbH
	WB	30 ±1	
Donaldson	D2	80	Donaldson
	D1	70	
	D4	40	

4.4.3 Porosity of the Membranes.

Because transport through the membrane is directly correlated to its volume porosity (table 9), which determines the volume to fill, the fiber volume fraction was measured, and the porosity was deduced. The porosity was calculated by

$$\varphi_{volume} = 1 - \frac{V_{fibers}}{V_{total}} \tag{1}$$

where ϕ_{volume} is the porosity of the membrane's sample, V_{fibers} is the volume occupied by the fibers in the sample, and V_{total} is the total volume of the sample.

Table 9. Porosity of Membranes

Manufacturer	Test Name	Porosity (%)	Source
W. L. Gore & Associates	W1	86% ±1%	Weight measurements
	WA	85 ±2%	W. L. Gore and Associates GmbH
	WB	85 ±2%	
Donaldson	D2, D1, D4	85 ±7%	Donaldson

4.4.3.1 Quantitative Characterization—Porometry.

The optical techniques described so far give relevant qualitative data about the morphology and the structure of the membranes. However, to fully understand the behavior of the membrane when implemented into a pressure-driven process, quantitative data are also required. Porometry techniques based on flow versus pressure measurements are able to provide this information. Recently, porometry has renewed interest among researchers [33-39]. The equipment used was a Capillary Flow Porometer from Porous Materials, Inc. [40]. The porometer provides information on pore size. As a first step, the classical pore information, such as the bubble point (BP) and the mean flow pore (MFP) (see definitions in sections 4.4.3.2.1 and 4.4.3.2.2), are gathered. But to capture the transport phenomena in the membrane, since they are dependent on the cumulative effects of the entire pore size distribution, the full range of the membrane's pore sizes had to be characterized. Therefore, the porometry data and the pore size distribution were fit appropriately. Zhao, et al. [41], and Metha, et al. [42], respectively, use a normal and a lognormal fit for the pore size distribution, while Rodgers, et al. [43], looked at numerous distributions. In this study, a Weibull distribution was the most appropriate. Moreover, because of the porometry limitations exposed in this study, this fit provided information beyond the limits of the porometer.

4.4.3.2 Discrete Information on Pore Sizes.

The first two parameters to be considered are the BP and the MFP of the membranes. Traditionally, both of them are provided by membrane manufacturers.

4.4.3.2.1 Bubble Point.

BP represents the largest constriction in the membrane detected by the porometer. It is important to indicate that the value is directly related to the smallest flow detectable by the porometer. It is, in fact, detected when the pressure increases incrementally to a level that is high enough to get initial flow through the membrane. Six replicates were measured for each membrane, as shown in table 10.

Table 10. Maximum Pore Size of Membranes

Membrane	BP (diameter) [40]	Standard Deviation [40]
W1	247	6.2
WA	425	20.6
WB	321	17.6
D2	566	19.31
D1	351	15
D4	220	12.7

4.4.3.2.2 Mean Flow Pore.

The MFP represents the pore size of which 50% of the flow Passes through pores smaller than the MFP and 50% passes through pores larger than the MFP. It is not related to the average of the pore size distribution. Six replicates were measured, as shown in table 11.

Table 11. The MFP Size of Membranes

Membrane	MFP (diameter) [40]	Standard Deviation [40]
W1	130	5.7
WA	254	3.5
WB	205	1.4
D2	256	9.8
D1	150	1.1
D4	101	2.4

4.4.3.3 Pore Size Distribution.

The pore size distribution is defined as the number of pores of each diameter. This is key information, since it is needed to calculate the transport characteristics of the membrane, such as its permeability. Starting from the wet and dry flow rates measured by the porometer, the flow fraction is determined following ASTM F316-03 [44]. Subsequently, the pore fraction was calculated and, assuming a certain total number of pores, an optimization was conducted to find the real number of pores in which the flow matched the raw data within the range detected by the porometer (figure 40).

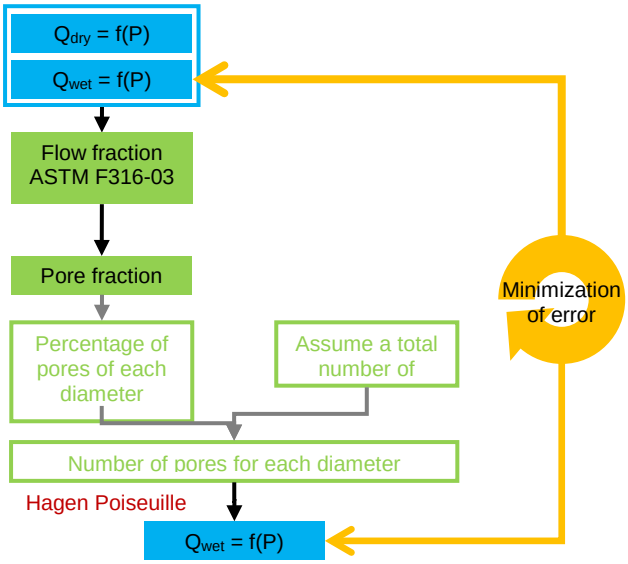

Figure 40. Methodology to Calculate the Pore Occurrences

4.4.3.4 Results of Pore Size Distribution.

Using the procedure in section 4.4.3.3, the pore size distributions of the six membranes studied were obtained (see figures 41 and 42). On both figures, the MFP is represented by a circle, and the BP is represented by a square. The former does not correspond to any particular feature of the distribution, and the latter is the last point on the plot since it was the first one to get detected by the porometer. It was observed that the MFP, apart from a flow indication, did not provide information in terms of the membrane's performance.

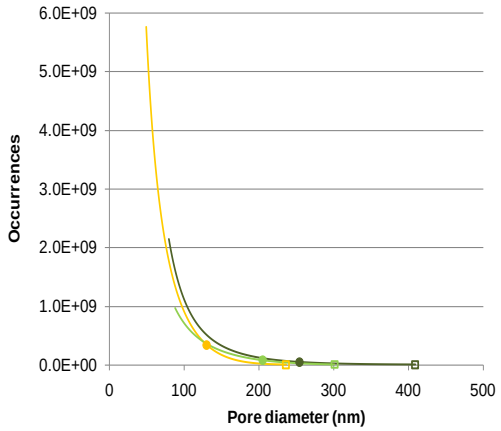

Figure 41. Pore Size Distributions of W1, WA, and WB

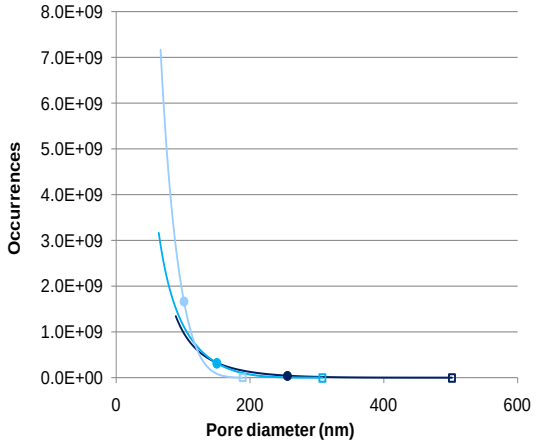

Figure 42. Pore Size Distributions of D2, D1, and D4

Looking at the different membranes (figures 41and 42), the membranes with the lowest BPs (W1 and D4) clearly have more pores toward the smaller range (below 100 nm). On the other hand, membranes with large BPs (D2 and WA) have very few small pores compared to the small BP membranes (W1 and D4). The decrease of occurrences toward the large pores is also less than for W1 and D4. So, an interesting attribute of the membranes is that having a larger BP does not mean that the distribution is simply translated towards larger pores. For instance, although

membranes WA and WB have larger BPs than W1, they have a very thin and elongated tail. The same observation can be made for D4, D1, and D2.

Comparing Donaldson's and W. L. Gore & Associates' membranes, it was observed that, although WA and D2 have almost the same MFP, their BPs differed significantly (figure 43). Likewise, D1 and WB have close BPs but very different profiles and MFPs. This again shows how the distributions of membrane can be different, and a single unique attribute is not sufficient to capture the membrane's behavior, especially in terms of transport.

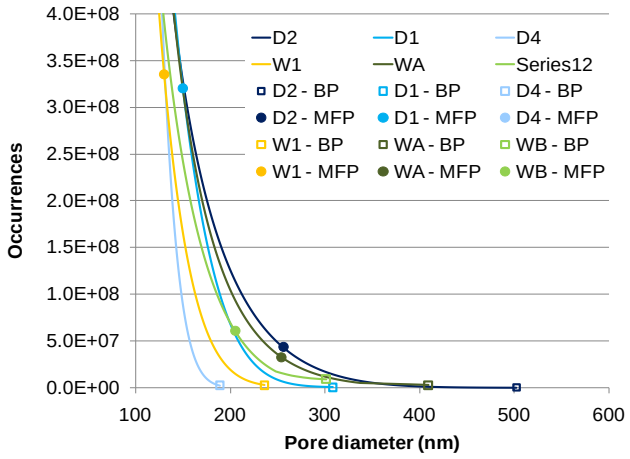

Figure 43. Pore Size Distributions of all Six Membranes

4.4.3.5 Statistical Fit of the Membranes' Pore Size Distribution.

Instead of directly fitting the pore size distribution obtained from the porometer, the statistical fit was optimized based purely on the flow information. The idea was to assume a distribution, then calculate its corresponding wet flow, compare it with the raw wet flow, and then iterate to find what statistical parameters gave the best fit between the calculated and raw flow rates.

The drawback of the first method (see section 4.4.3.3) was that the pore size would only be a partial distribution, because it was restricted to the range detectable by the porometer. Therefore, while the first method assumes that the data provided by the porometer covered the full range of pore sizes, the second method (described in this section) accounts for the limitations of the porometer and proposed fits beyond the porometer's limited range. The second method was therefore the most comprehensive. For the present applications, it became apparent that the best fit was the Weibull distribution (see table 12). The methodology is summarized in figure 44. All the calculations were conducted with the LabVIEW program, of which the interface is shown in figure 45.

Table 12. Probability Density and Cumulative Distribution Functions for the Weibull Fit

Probability Density Function	$\frac{\beta}{\alpha^{\beta}} d^{(\beta-1)} \exp\left(-\left(\frac{d}{\alpha}\right)^{\beta}\right)$ Equation 2	d = pore diameter α = scale parameter β = shape parameter
Cumulative Distribution Function	$1-\exp\left(-\left(\frac{d}{\alpha}\right)^{\beta}\right)$ Equation 3	

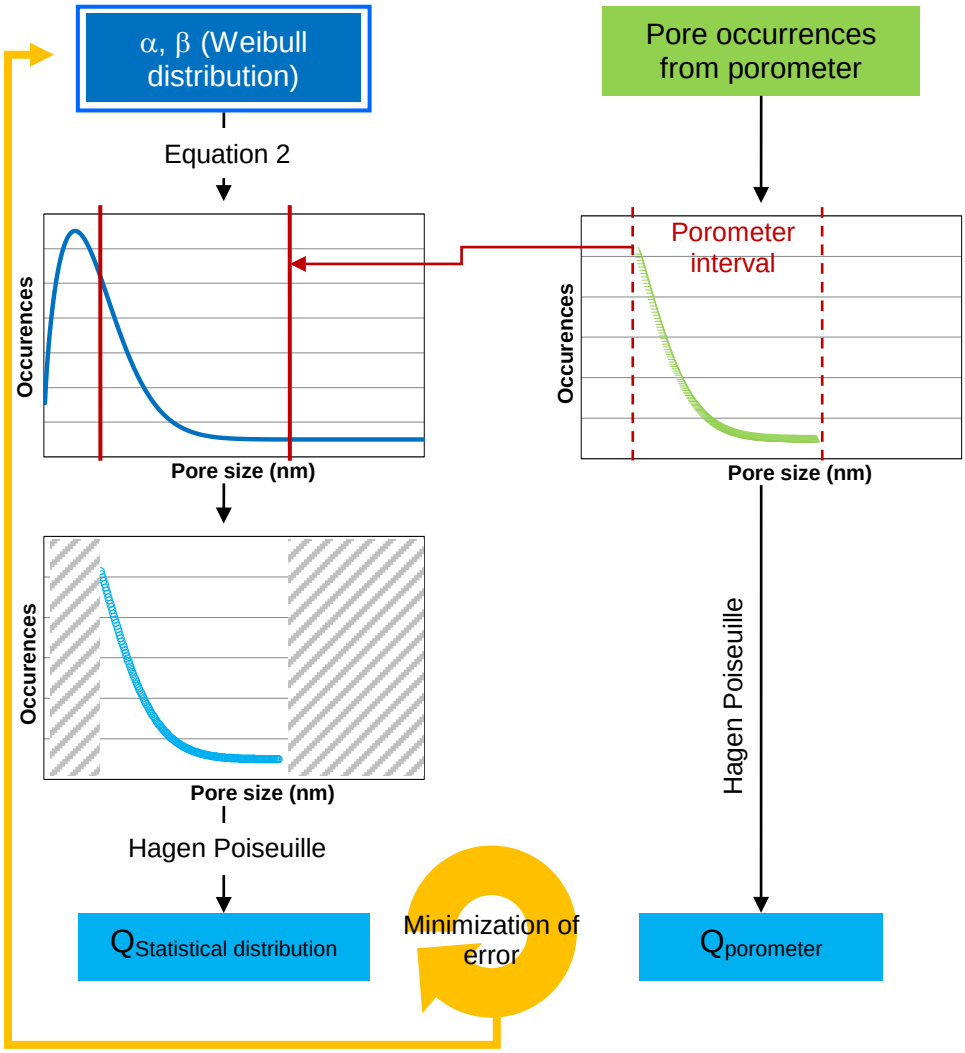

Figure 44. Optimization of Pore Size Distribution Through Fit of Flow Rates

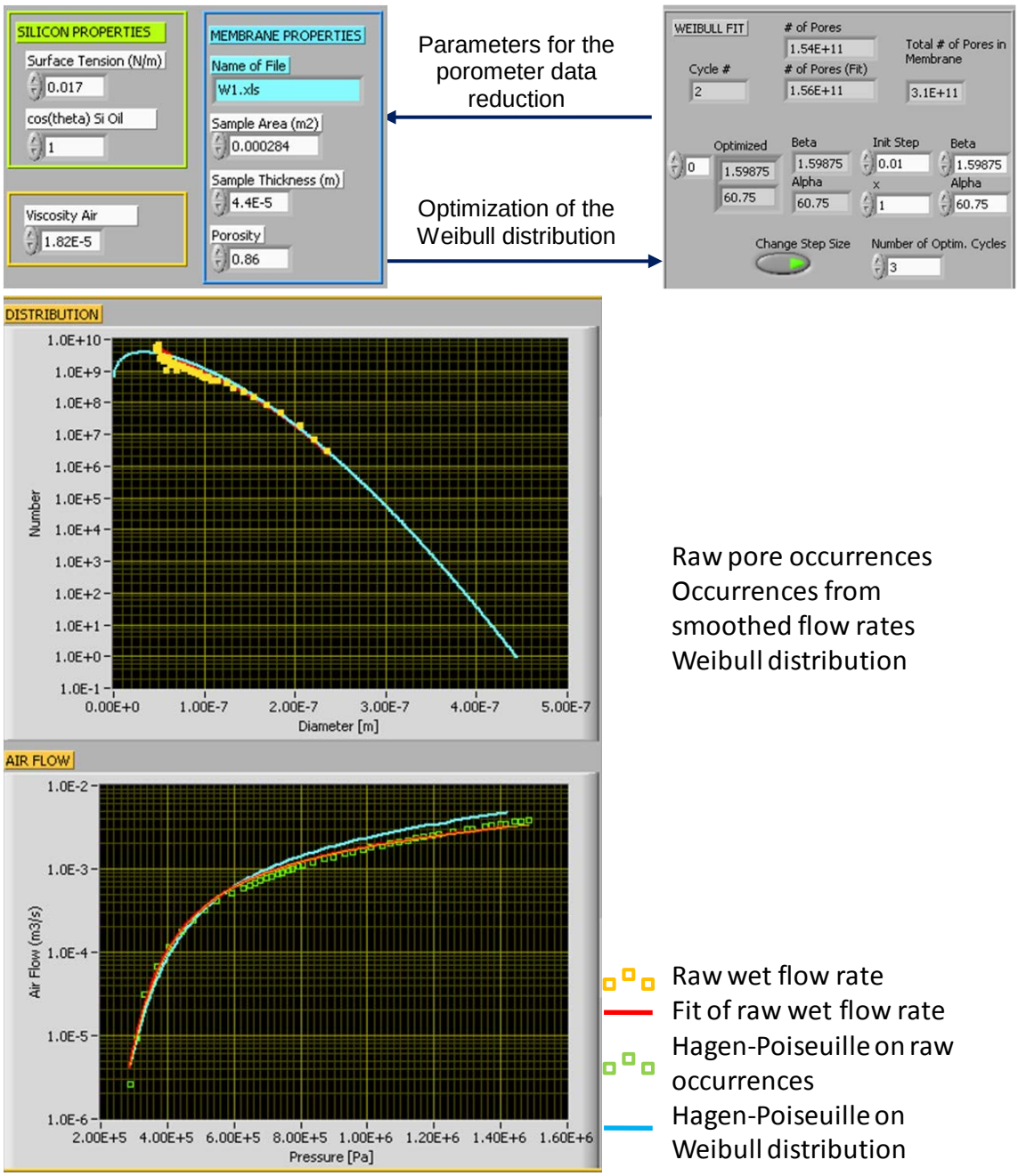

Figure 45. LabVIEW Interface to Obtain the Pore Size Distribution

The Weibull parameters for the different membranes are given in table 13.

Table 13. Weibull Parameters for All Membranes

Membrane	β (scale)	α (shape)
W1	60.75	1.6
WA	76.25	1.41
WB	77.25	1.71
D2	68.75	1.21
D1	67.25	1.51
D4	67	2.2

The pore size distributions for all membranes are shown in figures 46 through 48. Note that the MFP (represented by a circle) does not correspond to a particular feature of the distribution and is not at all representative of the right tail. On the other hand, the BP (represented by a square) is always in the very right tail of the distribution; in most cases, close to the last inflection point of the plot. For D2, both the BP and the inflection point almost overlap. In any case, the right tail follows the trend of the BP.

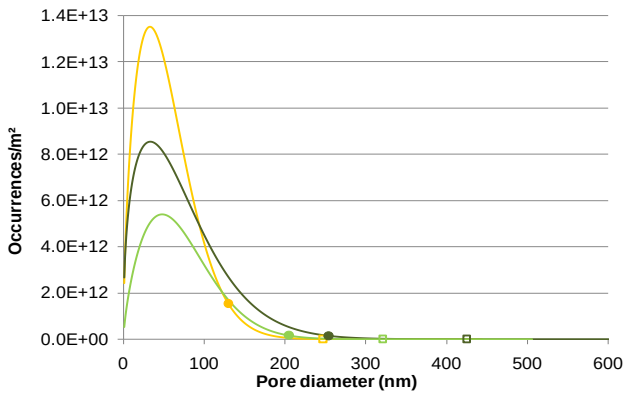

Figure 46. Pore Size Distribution for Membrane W

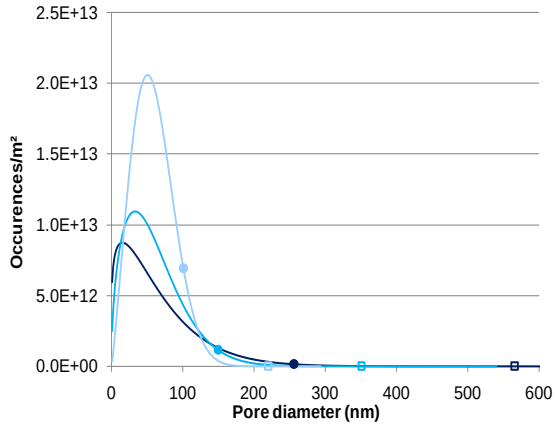

Figure 47. Pore Size Distribution for Membrane D

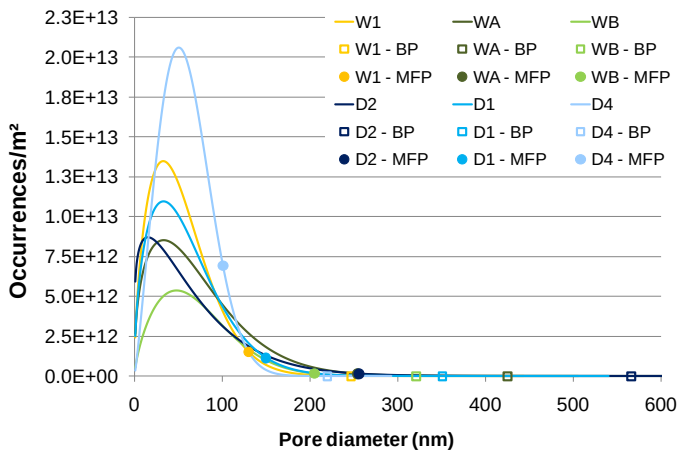

Figure 48. Pore Size Distribution for all Six Membranes

Looking at membrane W (figure 46), note that they all have their peak around 40 nm (30, 32, and 46 nm for W1, WA, and WB, respectively, while membrane D (figure 47) shows very different pore size value for their peak (15, 26, and 47 nm for D2, D1, and D4, respectively).

Comparing all membranes (figure 48), note that the larger the BP, the smaller the peak value. At the same time, the larger the BP, the wider the distribution. In fact, D4, the membrane with the lowest BP (220 nm), has the most narrow distribution. D2 and WA, which exhibit the largest BPs, have very similar distributions, especially toward the large pore size range. If this translates into similar membrane performance or if the difference in BP (425 nm for WA and 566 nm for D2) leads to dissimilar behaviors, additional research will be performed.

It was observed that the number of pores having the BP value was much higher for membrane W ($7x10^8$ to $5x10^9$) than for membrane D ($3x10^8$ to $9x10^7$). It was about one order of magnitude different, which may indicate that the pores with a diameter larger than the BP for the case of membrane W are less frequent and cannot contribute significantly to the overall flow that can be detected by the porometer. Membrane D may be composed of narrower distributions (smaller tail) in which the pores are larger than BP and more numerous but do not extend to the same range of pore sizes as membrane W.

4.4.4 Permeability of Membranes.

The work in reference 45 was dedicated to the calculation of the membrane permeability for a certain nonwetting fluid and membrane. For nonwetting fluids, the permeability was found to be pressure-dependent. Here, the results are extended to include all six membranes to complement the pore size distribution shown in figures 46 to 48. The calculation of permeability is based on a combination of the Hagen-Poiseuille equation and Darcy's Law. Therefore, some fluids' parameters are needed, along with the contact angle between the membrane and the fluids to calculate the pressure. The viscosity and the surface tension of water (testing fluid) and Cycom 977-20 epoxy resin are shown in table 14, and the contact angles of interest are shown in

table 15. The contact angle for WA was obtained experimentally, and the others were calculated based on an estimation of the membrane porosity.

Table 14. Viscosity and Surface Tension of the Fluids of Interest

Fluids	Viscosity (Pa·s)	Surface Tension (n/m)
HPLC	10^{-3}	$7.2 \times 10^{-2} \pm 0.7 \times 10^{-4}$
Cycom 977-20	120×10^{-3} at 167°F (75°C)	$3.5 \times 10^{-2} \pm 1 \times 10^{-4}$

HPLC = High-performance liquid chromatography
Pa·s = Pascal-second

Table 15. Contact Angles Fluids and Membranes

Membrane	HPLC	Cycom 977-20	Method
W1	118° ±5°	132°	Estimation based on porosity
WA	119° ±5°	132° ±2° (at infusion temperature)	Experimental (sessile drop method)
WB	118° ±5°	132°	Estimation based on porosity
D2	115° ±2°	128°	
D1	113° ±3°	126°	
D4	109° ±4°	122°	

The permeability of the six membranes was obtained with water (figure 49) and Cycom 977-20 resin (figure 50). As indicated previously, at very low pressures, the permeability is several orders of magnitude smaller than typical fabrics. Then, at a certain pressure, dependent on the fluid and the membrane, there is a rapid permeability increase leading to the third region, in which the permeability reaches a constant that corresponds to the steady-state flow of resin through the membrane (equal to the permeability for a membrane saturated with a wetting fluid).

These data provide a means to rank the membranes for any pressure-driven process. For example, in a process with a pressure of 5×10^5 Pa (figure 49), the membranes would rank as follows (from the best to the worst): D4 and W1, WB, D1, WA, and D2. In the D2 case, it would correspond to a permeability of about 10^{-16} m², which is three orders of magnitude smaller than a typical carbon fabric, whereas it would be 10^{-21} m² for WB.

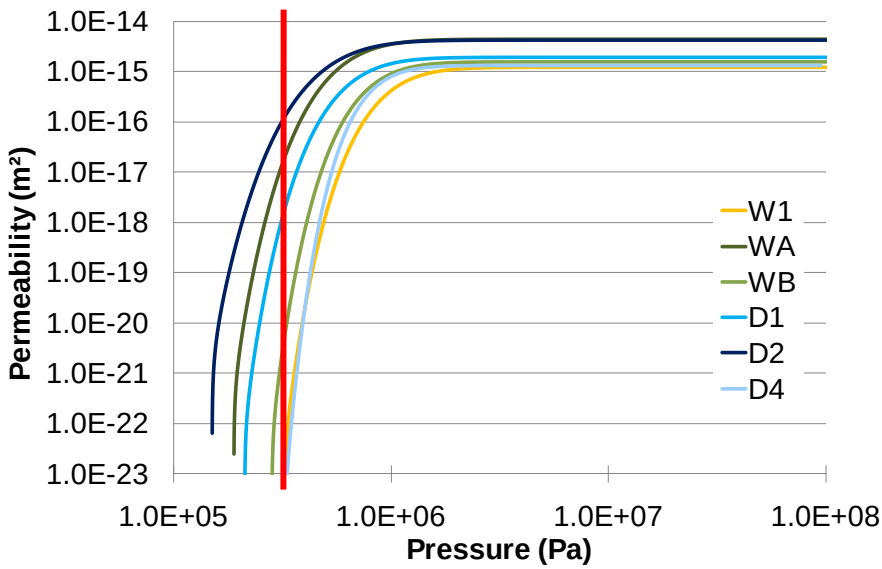

Figure 49. Permeability of the Six Membranes With Water

Looking at the data obtained for the Cycom 977-20 resin (figure 50), the permeabilities are larger for the same pressures due to the resin surface tension and contact angle differences from HPLC. Although the ranking is the same as water (D4 the best, then W1, WB, D1, WA, and D2 the worst), the permeabilities for 5 x 10^5 Pa (green line) are between 10^{-17} and $5x10^{-15}$ m².

Considering the VAP process, the only pressure to drive the fluid is vacuum that is 10^5 Pa (red line). At this level, all membranes except D2 have a permeability more than ten orders of magnitude smaller than a typical carbon fabric. Therefore, it was concluded that they should all provide barrier properties with the nonwetting resin except D2, which would be predicted to have resin transport at this pressure. Future work will take into consideration time to determine an acceptable level of leakage. In fact, an important parameter to consider is the resin gel time, which can vary from minutes to hours to days. The membrane must work over this timeframe as either a total barrier or limit the flow rate to an acceptable level. In this respect, the membrane process window can be relaxed, since the membrane can leak and does not need to work indefinitely.

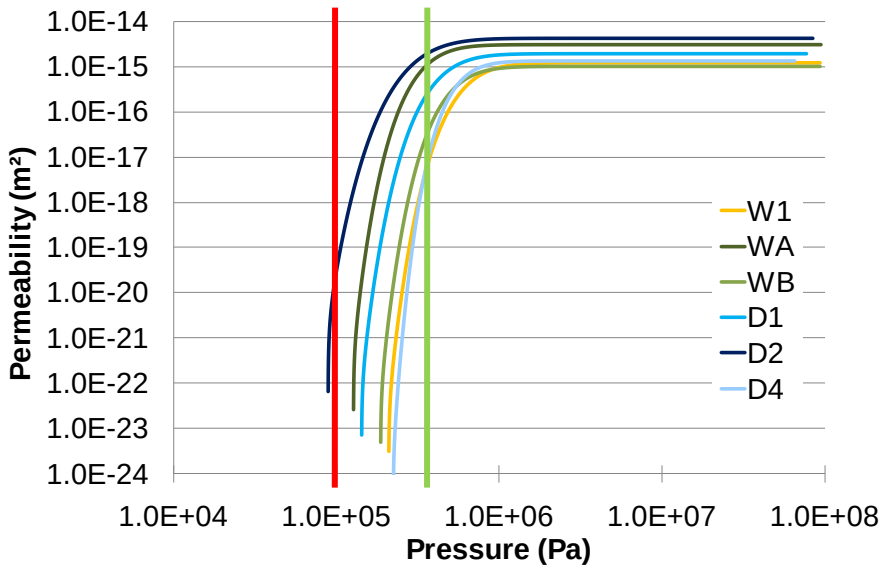

Figure 50. Permeability of the Six Membranes With Cycom 977-20 Resin

A full characterization of six membranes that could be considered as candidates for VAP was implemented. First, the membranes' morphology was observed using classical means, such as optical and SEM. This qualitative characterization was followed by quantitative characterization using porometry. Although the porometer provides some discrete information, such as the MFP size, BP, and a pore size distribution, the entire distribution was statistically fit. This allows getting beyond the porometer limitations and to capture the membranes' behavior in pressure and flow ranges not necessarily covered by the porometer but of great relevance to the success of membrane-based composite processing.

5. ELEVATED TEMPERATURE VARTM PROCESSING.

This section describes the development of an Elevated Temperature VARTM (ET-VARTM) station to process elevated temperature epoxy matrices for aerospace applications. The goal is to gain laminate qualities comparable to prepreg autoclaving by using modified prepreg resins and taking advantage of simplicity and cost effectiveness of the vacuum infusion process.

5.1 MATERIALS.

The specified and certified single-component epoxy resin systems made the processing at elevated temperature necessary. Their viscosities are too high at room temperature to be used in vacuum infusion and their cure is temperature-initiated (~350°F).

Cytec Cycom 977-20 is derived from a prepreg-specific, toughened epoxy system (Cycom 977-2). To tailor the resin to infusion processes, thermoplastic toughening agents were removed to lower viscosities. The system is mainly used in RTM processing in combination with Cytec PriForm™ fabric, which includes the toughening agent as intermingled, soluble

thermoplastic yarns. Thus, a dissolution stage is necessary before the cure cycle. The temperature profile recommended for this resin system is shown in figure 51.

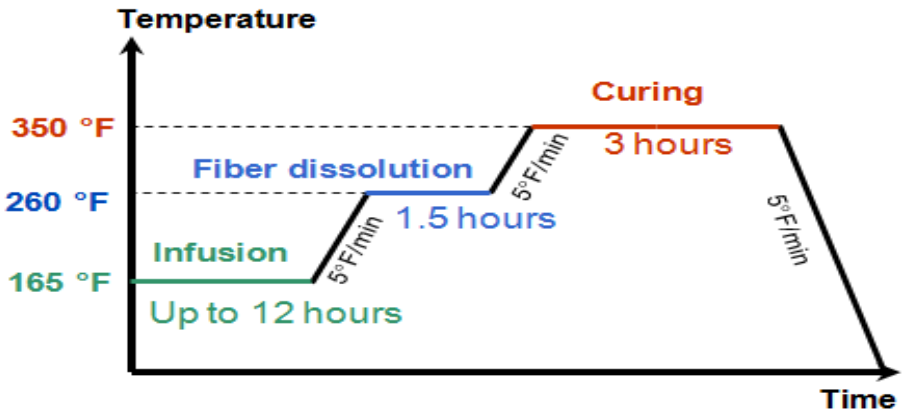

Figure 51. Process Temperature Profile for Cycom 977-20 With PriForm Reinforcement

Hexcel RTM6 is an epoxy system commonly used in RTM processing as well. It features a viscosity profile and curing properties similar to Cycom 977-20. Hexcel RTM6 does not include toughness-enhancing additives. Hexcel SGP196P is a commonly used, intermediate modulus carbon fiber fabric (IM7GP 6K) in plain weave configuration with an aerial weight of 196g/m^2. Cytec PriForm is a proprietary hybrid fabric in four-harness weave with Toho/Tenax HTA 6k 5131 carbon fibers and intermingled thermoplastic, soluble yarn running parallel to the carbon tows in the warp direction.

5.2 EXPERIMENTAL SETUP.

Using the computerized ET-VARTM work cell (see figure 52) allowed the monitoring and control of the two main process parameters (i.e., temperature and pressure) at all stages in the process. The system was designed with focus on the high variability of processing scenarios, real-time monitoring and control, and safety aspects concerning highly reactive resins.

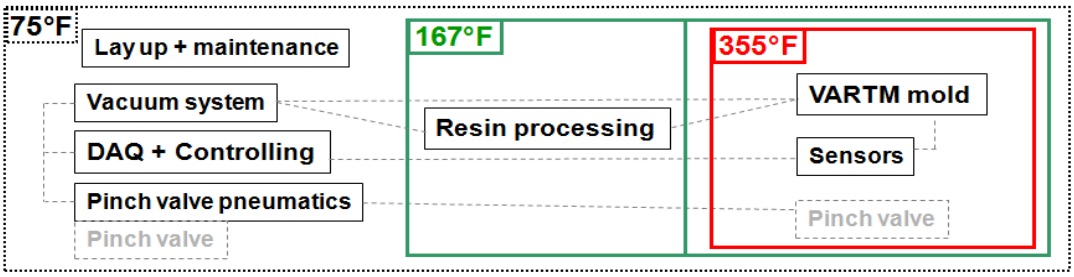

Figure 52. The ET-VARTM Work Cell Schematic

Handling of liquid resin was reduced to filling the preheating chamber, from which it will later flow directly into the preheated mold cavity. The resin was also degassed in the reservoir before infusion. The mold inside the oven was connected to the resin chamber by a heated tube. Resin flow was stopped and started using a vise or pneumatic grippers. The weight of the infused resin

was measured by a balance under the reservoir and fed into the LabVIEW interface. Pressure levels in the mold and reservoir could be independently adjusted to allow for varying processing scenarios, i.e., CAPRI processing.

One critical characteristic of single-component resin systems is the significant drop in viscosity, up to an order of magnitude, before cross-linking occurs at curing temperature, as shown in figures 53 and 54. This is the reason the best approach is likely to infuse quickly and saturate the fiber capillaries postinfusion.

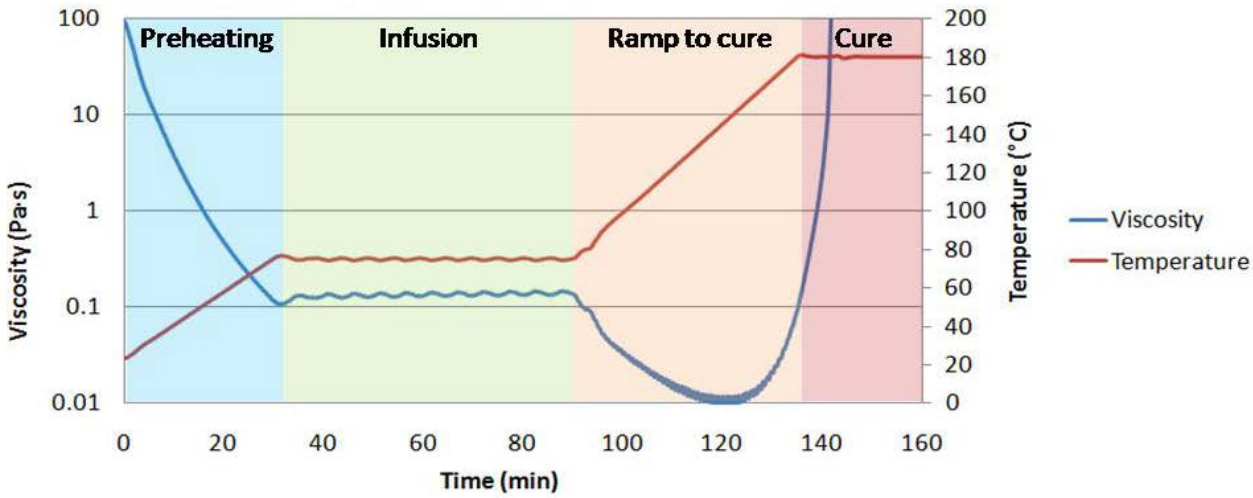

Figure 53. Viscosity Profile of Cycom 977-20 During Two-Step Temperature Cycle (no thermoplastic fiber dissolution phase)

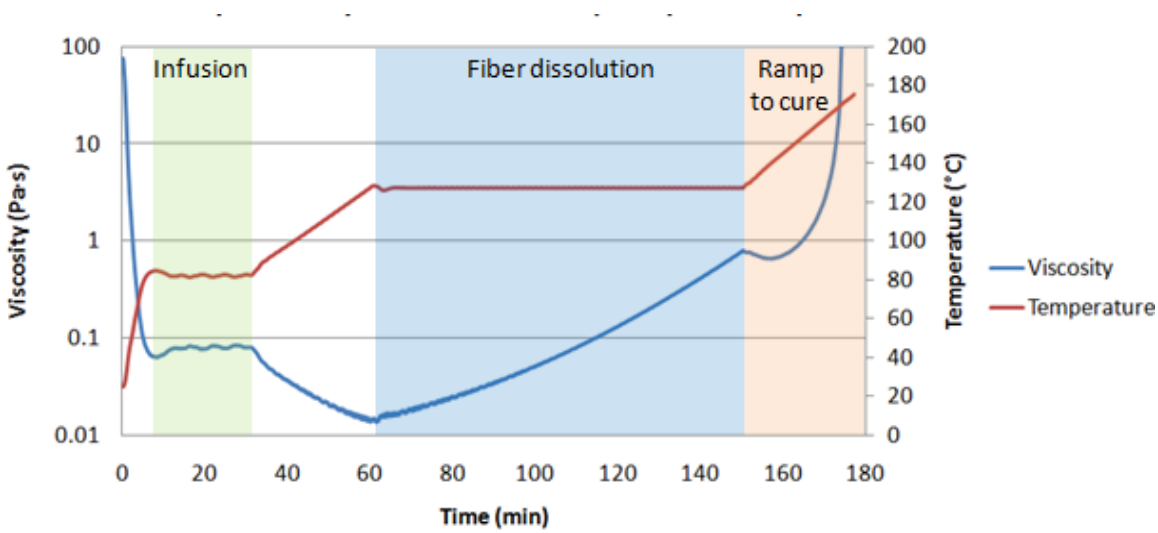

Figure 54. Viscosity Profile of Cycom 977-20 During Three-Step Temperature Cycle (with thermoplastic fiber dissolution phase)

Accelerating and stabilizing flow velocity in the later stage of infusion can be done by continuously increasing the temperature during the infusion phase, thus decreasing resin viscosity and balancing the characteristic reduction in flow speed during vacuum infusions.

The literature indicates the existence of an optimum flow rate in liquid-molding processes to minimize macro- and microvoid formation [46]. Void formation is strongly related to the balance of bulk and capillary flow conditions. High resin flow rates primarily create microvoids due to dominant viscous flow surpassing capillary flow and entrapping volatiles inside the fiber tows. Low flow rates create macrovoids between tows due to dominant advancing capillary flow entrapping volatiles between saturated fiber tows. The observation of high-macrovoid development indicated that infusion speeds of the initial ET-VARTM scenario had to be increased to reach the micro- and macroflow equilibrium. The described postinfusion drop in viscosity amplifies the already dominating capillary flow. Unfilled macrovoids will not be filled or moved out of the laminate in this stage.

Resin viscosity characteristics at elevated temperatures were studied, and it was found that the resin systems in question exhibited sufficient working times even at higher processing temperatures than recommended by the manufacturers (~170°F). Both resin systems stayed well below the infusion viscosity threshold of 1 Pa·s for at least 5 hours at 200°F. This encouraged shifting the infusion phase into higher-temperature regions, particularly the ramp-to-dissolve/cure phase (see figure 55).

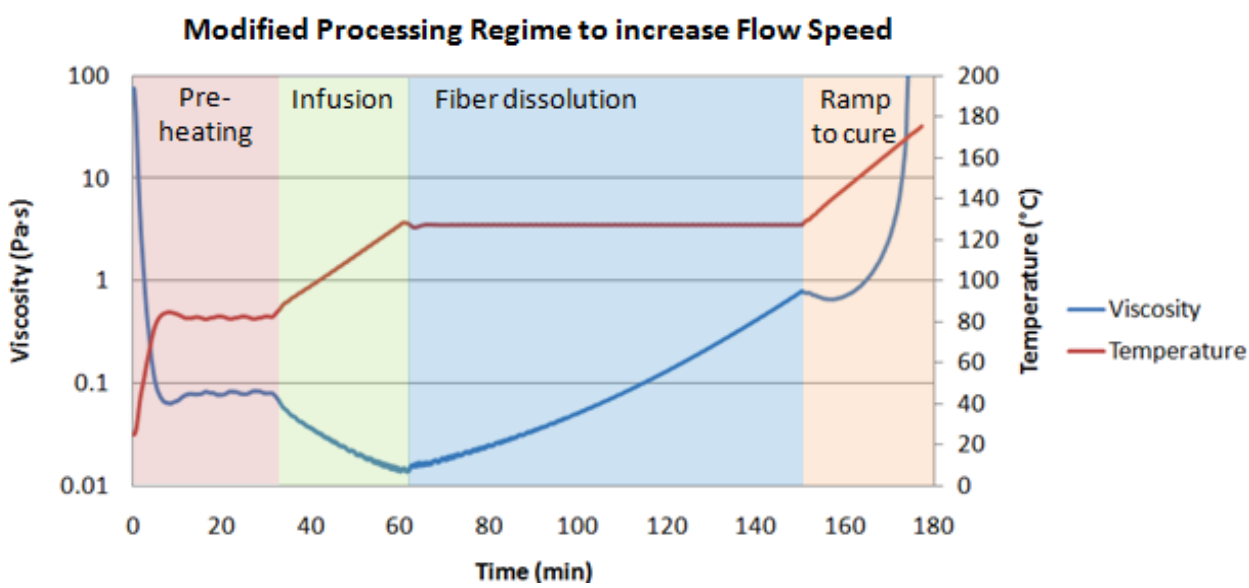

Figure 55. Viscosity Profile of Cycom 977-20
(infusion phase shifted into higher-temperature region)

Test infusions implementing the increased and progressive flow speed scenario showed significant reduction of void formation in saturated areas (see figure 56). Currently, the temperature regime is being optimized to balance viscosity and curing behavior for both resin systems so the minimum viscosity is reached before flow velocity decreases due to complete

infusion of the preform. The effect of lowered viscosity on balance of micro- and macroflow is left for future work to eliminate the potential of shifting void formation into the microscale or fiber tows.

Figure 56. Initial Laminate Quality Showing Heavy Macrovoid Formation (left) and Improved Laminate Quality With Virtually No Void Formation (right) After Increasing Infusion Speed

5.3 MECHANICAL TESTING—MATERIAL PROPERTIES.

Test panels of different fiber-matrix combinations were manufactured in a flow speed-optimized SCRIMP configuration. Cycom 977-20 was paired with the recommended Cytec PriForm material, as well as the more generic Hexcel SGP196P fabric. Hexcel RTM6 was only infused into Hexcel SGP196P. As first indicators of high-quality laminates, fiber volume fractions of ~55% were achieved in all panels. Mechanical test results obtained from respective ASTM standard tests are summarized in table 16.

Table 16. Mechanical Test Results

	Fiber Volume Fraction (%)	Compression Strength ASTM D3410 (ksi)	Tensile Strength ASTM D3039 (ksi)	Short-Beam Shear Strength ASTM D2344 (ksi)	Open-Hole Compression Strength ASTM D6484 (ksi)	Open-Hole Tensile Strength ASTM D5766 (ksi)
Cycom 977-20 + Hexcel SGP196P	55.8	65.5 ±4.8	84.3 ±3.7	9.9 ±0.5	44.2 ±1.2	50.6 ±3.7
977-20 + PriForm	55.6	66.4 ±3.4	65.9 ±2.9	9.9 ±0.6	45.6 ±1.2	44.5 ±1.5
RTM6 + Hexcel SGP196P	53.2	56.9 ±3.3	68.9 ±3.8	8.8 ±0.6	*	*
Cycon977-2 Prepreg	*	*	*	11.9	43.6	*

* = to be executed/not available

The level of mechanical performance using the optimized process was shown to approach prepreg levels. Although PriForm is exclusively specified for Cycom 977-20, it exhibited less performance in fiber-dominated load cases (tension) than Hexcel SGP196P laminates. As expected from a toughened system, it showed excellent properties in matrix-dominated load cases, such as shear and compression.

6. CONCLUSIONS.

The Vacuum-Assisted Resin Transfer Molding (VARTM) process has developed over the last 20 years and has been successfully demonstrated in marine, wind, and aerospace applications. This report reviewed some of the basic fundamental processing science and presented basic analytical models to simulate the infusion as well as thickness behavior during and after infusion. These models are used to capture the process physics and provide guidance when the material or geometry is changed.

Three process variations, including Seeman Composites Resin Infusion Molding Process (SCRIMP), Vacuum-Assisted Process (VAP) and Controlled Atmospheric Pressure Resin Infusion (CAPRI), were evaluated in detail. Each has a unique setup, as outlined in this report, and each process has advantages and disadvantages. The use of a distribution media in the SCRIMP processes allowed infusion of large components. Partial vacuum and debulking in the CAPRI process improved final properties and reduced variation. The VAP process is certified for commercial aerospace applications and reduces void content to a minimum.

Mechanical properties of toughened aerospace-grade epoxy composites were evaluated for VARTM. The properties are comparable to autoclave prepreg, except the maximum fiber volume fraction is limited to the compaction under vacuum only.

7. REFERENCES.

1. Hexcel RTM 6 Product Data Sheet: http://www.hexcel.com/resources/datasheets (last visited 9/19/12).

2. Cytec Cycom 977-20 Product Data Sheet: http://www.cytec.com/engineered-materials /products/Datasheets/PRIFORM_CYCOM_977-20_RTM.pdf (last visited 11/21/11).

3. Henkel Henkel Benzoxazine 99110 Product Data Sheet: http://www.henkel.com/ com/content_data/180355_Benzoxazine_Resin_99110_Final.pdf, (last visited 7/17/12).

4. Cocquyt, A., “The VIP Primer,” http://www.grpguru.com/vipupdate.asp (last visited 8/30/12).

5. Seeman II, United States Patent 4,902,215, 1990.

6. TPI Composites, Inc., http://www.tpicomposites.com/innovation/patents.aspx

7. Bruschke, M.V. and Advani, S.G., “A Numerical Approach to Model Non-Isothermal Viscous Flow Through Fibrous Media With Free Surfaces”, *International Journal of Numerical Methods in Fluids*, Vol. 19, October 1994.

8. Bruschke, M.V. and Advani, S.G., “A Finite Element/Control Volume Approach to Mold Filling in Anisotropic Porous Media,” *Polymer Composites*, Vol. 11, 1990.

9. Bruschke, M.V. and Advani, S.G., *SAMPE Quarterly*, 1990.

10. Liu, D., Bickerton, S., and Advani, S.G., *Composites Part A*, 27A, 1996.

11. Mohan, R.V., Ngo, N.D., Tamma. K.K., and Fickie, K.D., *Polymer Engineering and Science*, Vol. 39, No. 1, 1999.

12. Trochu, F., Gauvin, R., Gao, D.M., and Boudreault, J-F., *Journal of Reinforced Plastics and Composites*, Vol. 13, No. 3, 1994.

13. Lee, L.J., Young, W.B., and Lin, R.J., *Composite Structures*, Vol. 27, No. 1-2, 1994.

14. Simacek, P., Sozer, E.M., and Advani, S.G., “User Manual for DRAPE 1.1 and LIMS 4.0,” Technical report, Center for Composite Materials, University of Delaware, 1998.

15. Gallez, X.E. and Advani, S.G., *Proceedings of the Fourth International Conference on Flow Processes in Composite Materials*, University of Wales, 1996.

16. Tari, M.J., Imbert, J-P., Lin, M.Y., Lavine, A.S., and Hahn, H.T., *Journal of Manufacturing Science and Engineering*, Vol. 120, 1998.

17. Hsiao, K.T., Mathur, R., Gillespie, J.W., Fink, B.K., and Advani, S.G., *ASME Journal of Manufacturing Science and Technology*, May 2000.

18. Heider, D., Hofmann, C., and Gillespie, J.W., Jr., *Proceedings of the 45rd International SAMPE Symposium/Exhibition*, 2000.

19. Heider, D.; Graf, A., Fink, B.K., and Gillespie, J.W., Jr., *Proceedings of SPIE - The International Society for Optical Engineering*, 3589, 1999.

20. Gillespie, J.W., Fink, B.K., and Don, R.C., “Low-Cost Distributed Sensors for Flow and Cure Monitoring in Resin Injection Molding Processes,” disclosure completed, April 1997.

21. Fink, B.K., Walsh, S.M., DeSchepper, D.C., McCullough, R.L., Don, R.C., Waibel, B.J., and Gillespie, J.W., Jr., *Proceedings of the ASME Materials Division*, 69-2, 1995.

22. Nedanov, P., Advani, S.G., Walsh, S.M., and Ballata, B.O., *Proceedings of the ASME, Advances in Aerospace Materials and Structures*, 58, 1999.

23. ASTM D2584, "Standard Test Method for Ignition Loss of Cured Reinforced Resins."

24. Woods, J., Modin, A.E., Hawkins, R.D., Hanks, D.J., "Controlled Atmospheric Pressure Infusion Process," International Patent WO 03/101708 A1

25. Chen, B. and Chou, T.W., "Compaction of Woven-Fabric Preforms in Liquid Composite Molding Processes: Single-Layer Deformation," *Compos Sci Technol*, 59, 1999, pp. 1519-1526.

26. Robitaille, F. and Gauvin, R., "Compaction of Textile Reinforcements for Composites Manufacturing. II: Compaction and Relaxation of Dry and H2O-Saturated Woven Reinforcements," *Polym Compos*, 19, 1998, pp. 543-557.

27. Zhang, Y., Scholtz, S., Amouroux, S., Gillespie, J.W., Jr., and Heider, D., "Measurement of Transverse Permeability Using Gaseous and Liquid Flow," *Proceedings of the American Society for Composites 20th Technical Conference*, Philadelphia, Pennsylvania, 2005.

28. Gore Membrane Information, http://www.gore.com/en_xx/products/filtration/micro/gore_microfiltration_media.html

29. ASTM D3171-99, "Standard Test Methods for Constituent Content of Composite Material."

30. ASTM D2734-94, "Standard Test Method for Void Content of Reinforced Plastics."

31. ASTM D2344, "Standard Test Method for Short-Beam Strength of Polymer Matrix Composite Materials and Their Laminates."

32. Donaldson Membrane Information, http://www.donaldson.com/en/filtermedia/support/datalibrary/003703.pdf, last visited 07/18/12.

33. Brun, M., et al., "New Method for Simultaneous Determination of Size and Shape of Pores—Thermoporometry," *Thermochimica Acta*, 21(1), 1977, pp. 59-88.

34. Jena, A. and Gupta, K., "Characterization of Water Vapor Permeable Membranes. Desalination, 149(1-3), 2002, pp. 471-476.

35. Jena, A. and Gupta, K., "An Innovative Technique for Pore Structure Analysis of Fuel Cell and Battery Components Using Flow Porometry," 2001, Manchester, *Elsevier Science B.V.*

36. Jena, A. and Gupta, K., "Characterization of Pore Structure of Filtration Media," *Fluid Particle Separation Journal*, 4(3), 2002, pp. 227-241.

37. Martinez, L., et al., "Characterisation of Three Hydrophobic Porous Membranes Used in Membrane Distillation: Modelling and Evaluation of Their Water Vapour Permeabilities," *Journal of Membrane Science*, 203(1-2), 2002, pp. 15-27.

38. Mayer, E. and Warren, J., "Evaluating Filtration Media—A Comparison of Polymeric Membranes and Nonwoven," *Filtration and Separation Journal*, 35(10), 1998.

39. Mietton-Peuchot, M., Condat, C., and Courtois, T., "Use of Gas-Liquid Porometry Measurements for Selection of Microfiltration Membranes," *Journal of Membrane Science*, 133(1), 1997, pp. 73-82.

40. Porous Materials, Inc.: www.pmiapp.com

41. Zhao, C., Zhou, X., and Yue, Y., "Determination of Pore Size and Pore Size Distribution on the Surface of Hollow-Fiber Filtration Membranes: A Review of Methods," *Desalination*, 129(2), 2000, pp. 107-123.

42. Mehta, A. and Zydney, A.L. "Permeability and Selectivity Analysis for Ultrafiltration Membranes," *Journal of Membrane Science*, 249(1-2), 2005, pp. 245-249.

43. Rodgers, V.G.J. and Derjani-Bayeh, S. "Sieving Variations Due to the Choice in Pore Size Distribution Model," *Journal of Membrane Science*, 209(1), 2002, pp. 1-17.

44. ASTM F316, "Standard Specification for Wrought Titanium 6Aluminum 4Vanadium ELI (Extra Low Interstitial) Alloy for Surgical Implant Applications (UNS R56401).

45. Amouroux, S.C., "On the Role of Membrane to Improve Quality of VARTM Processed Composites," *SAMPE Journal*, 42(1), 2006. pp. 31-40.

46. Ruiz, E., Achim, V., Soukane, S., Trochu, F., and Bréard, J., "Optimization of Injection Flow Rate to Minimize Micro/Macro-Voids Formation in Resin Transfer Molded Composites," *Composites Science and Technology*, Vol. 66, Issues 3-4, March 2006, pp. 475-486.